Carlton Rhyolite Group and diabase intrusions in the East Timbered Hills, Arbuckle Mountains

Amy M. Eschberger[1], Richard E. Hanson[2], and Robert E. Puckett, Jr.[3]

[1]*School of Geology, Energy, and the Environment, Texas Christian University, Fort Worth, Texas 76129. Current address: Colorado Department of Natural Resources, Division of Reclamation, Mining, and Safety, 1313 Sherman Street, Suite 215, Denver, Colorado 80203. aeschberger@yahoo.com.*

[2]*School of Geology, Energy, and the Environment, Texas Christian University, Fort Worth, Texas 76129. r.hanson@tcu.edu. Corresponding author.*

[3]*12700 Arrowhead Lane, Oklahoma City, Oklahoma 73120. bpuckett@priceedwards.com.*

INTRODUCTION

Rhyolites in the Arbuckle Mountains were mapped by Taff (1904) and later described by Uhl (1932). Our work represents the first modern, detailed study of the rhyolites. These rocks were originally named the Colbert porphyry by Reeds (1910). However, because subsurface data show the Arbuckle rhyolites to be a direct continuation of the Carlton Rhyolite exposed in the Wichita Mountains, it seems unnecessary to give a separate lithostratigraphic name to the examples exposed in the Arbuckles, and we follow Ham et al. (1964) in referring to all these rocks as parts of the Carlton Rhyolite Group.

The rhyolites crop out in the western part of the Arbuckle Mountains in the East and West Timbered Hills (Figs. 1 and 2). Our work has focused on the Carlton Rhyolite exposed in the East Timbered Hills (ETH), as discussed in this paper, and on an unusual igneous breccia within the rhyolite in the West Timbered Hills, which is discussed in Eschberger and Hanson (this guidebook). Diabase intrusions occur in both areas, and we also present new data on these rocks. For a more thorough discussion of the new findings than is possible here, the reader is referred to Eschberger (2012).

The closest well to the outcrops in the ETH that penetrates the Carlton Rhyolite in the subsurface is the Kaiser Francis-Westheimer Neustadt 1 Chapman (hereafter referred to as the KFWNC well), which was drilled in 1980 to a total depth of 2.34 km and lies 3.3 km southeast of the rhyolite exposures (Figs. 1 and 2). Igneous rocks penetrated by this well have not been described in detail before, and Eschberger (2012) carried out petrographic and geochemical studies of rhyolite cuttings from the well. One goal of this part of the project was to determine whether stratigraphic relations shown by the rhyolites in outcrop could be carried into the subsurface, and we briefly summarize results of this work in the present paper.

The rhyolites in the East and West Timbered Hills are exposed within two structural culminations in the core of the Arbuckle Anticline, which is an asymmetric, northeast-verging structure delimited by the Washita Valley Fault Zone along its steep northern flank (Fig. 2; Ham, 1973; Perry, 1989). Mesoproterozoic granite and gneiss of the Eastern Arbuckle Province are exposed on the northern side of the fault zone (Fig. 1; Ham et al., 1964; Rohs and Van Schmus, 2007). Ham et al. (1964) showed that units belonging to the Carlton Rhyolite Group form a succession at least 1.5 km thick in the subsurface south of the Washita Valley Fault Zone, based on information from the Frankfort 1 Sparks Ranch well (Figs. 1 and 2). This is in contrast to the complete absence of extrusive rhyolites north of the fault zone. Because the rhyolites south of the fault zone and crystalline basement of the Eastern Arbuckle Province north of the fault zone are both unconformably overlain by the Upper Cambrian Reagan Sandstone, Ham et al. (1964) inferred that the Washita Valley Fault Zone originated as a pre-Reagan, synvolcanic normal fault. This fault contained the rhyolites on the basinward side and was subsequently reactivated as a compressional structure during Pennsylvanian deformation. More recent subsurface work to the northwest of the exposures in the Arbuckle Mountains has further emphasized the great thickness of volcanic rocks that accumulated south of this Cambrian normal fault (Puckett, 2011; Puckett et al., this guidebook).

CARLTON RHYOLITE GROUP IN THE EAST TIMBERED HILLS

Rhyolite outcrops in the ETH are delimited to the north by a northwest-striking thrust fault that is a strand of the

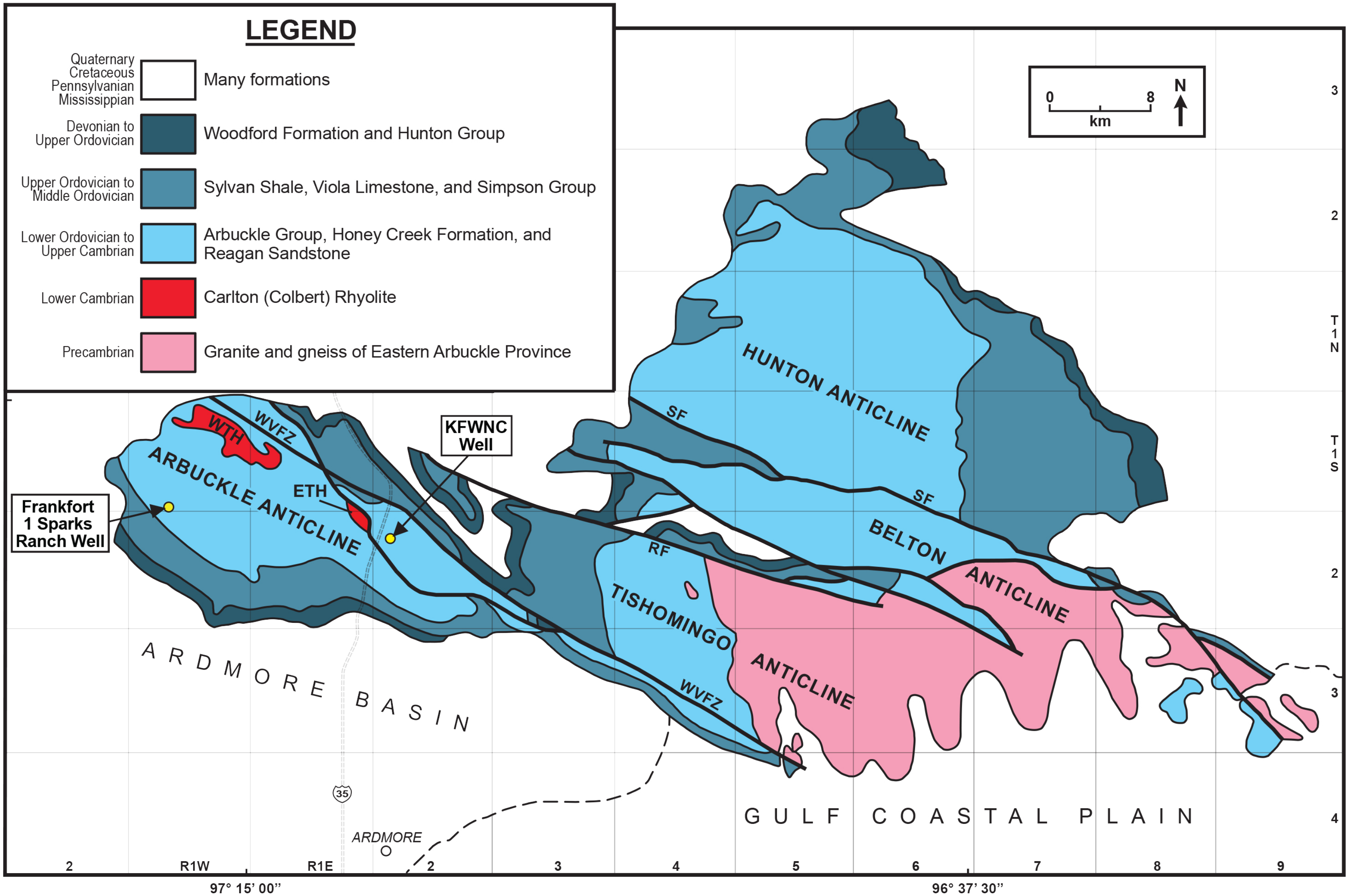

Figure 1. Geologic map of the Arbuckle Mountains, modified from Ham (1973). Locations of Kaiser Francis-Westheimer Neustadt 1 Chapman (KFWNC) well and Frankfort 1 Sparks Ranch well are indicated. WTH: West Timbered Hills; ETH: East Timbered Hills; WVFZ: Washita Valley Fault Zone; RF: Reagan Fault; SF: Sulphur Fault. WVFZ separates western Arbuckle Mountains (including Arbuckle Anticline) from eastern Arbuckle Mountains (including Tishomingo, Belton, and Hunton Anticlines).

Washita Valley Fault Zone and places the rhyolite against Cambrian-Ordovician carbonate rocks of the Arbuckle Group (Figs. 2 and 3). To the east, the rhyolites are faulted against Arbuckle Group strata along the Chapman Ranch Thrust Fault (Ham and McKinley, 1954). The unconformity between the rhyolites and the overlying Reagan Sandstone is exposed in the western part of the area, and thin fault slices of the sandstone also occur along the thrust fault to the northeast.

Our mapping shows that the Carlton Rhyolite in the ETH consists predominantly of two thick lava flows separated by an interval of bedded rhyolitic volcaniclastic rocks and intruded by a series of hypabyssal felsic intrusions (Fig. 3). Field relations and petrographic features of these units are discussed below. The total stratigraphic thickness of exposed rhyolite is ~960 m, as shown in the cross section (Fig. 4), which was constructed using bedding attitudes from the volcaniclastic rocks separating the two flows.

In addition to the thrust faults that bound the rhyolite to the north and east, several smaller faults cut the rhyolite and offset the bedded volcaniclastic rocks in a complex manner (Fig. 3). A number of brittle shear zones with variable trends and unknown displacement also occur within the rhyolite, as shown in Figure 3, and are as much as 80 m across. They are defined by closely spaced, sub-parallel, steeply dipping fractures that locally grade into pockets of fine-grained cataclasite (Figs. 5A and 5B), and some polished fracture surfaces exhibit slickenlines. These shear zones are inferred to record brittle deformation of the rhyolites during Pennsylvanian folding and faulting.

Lower rhyolite flow

The lower rhyolite flow is only exposed in the eastern part of the study area and is largely bound by faults (Fig. 3). The flow is >300 m thick, but its true thickness is unknown because the base is truncated by the Chapman Ranch Fault. It is aphyric and pervasively flow banded down to thin-section scale (Figs. 6A and B). Pink or tan bands alternate with dark-gray bands, and spherulites consisting of radiating microlites of quartz and alkali feldspar are abundant in the pink and tan bands (Figs. 6C and 6D). In contrast, the dark-gray bands exhibit relict perlitic texture (Fig. 7A) overprinted by a very fine grained mosaic of anhedral, equidimensional quartz and feldspar. Following reasoning given in Hanson et al. (this guidebook), we infer that the spherulites in the pink and tan bands formed during high-temperature devitrification while the flow underwent initial cooling from magmatic temperatures after it came to rest. The presence of perlitic texture in the dark-gray bands indicates that these bands originally remained largely glassy following initial cooling of the lava and underwent slow, long-term devitrification well after the flow had cooled to ambient temperatures. In the dark-gray bands, delicate flow lamination is defined by opaque crystallites (Fig. 6B), and some of these bands also contain abundant small, elongate amygdules oriented in the direction of flow and filled with quartz (Fig. 7B). Fine-grained secondary quartz replaces parts of the groundmass in small, irregular patches (Fig. 6B), and some spherulites have recrystallized entirely to quartz, leaving only traces of the original fibrous, radiating structure (Fig. 7C).

Open to isoclinal flow folds from thin-section to outcrop scale commonly deform the flow banding (Figs. 6B and 8A and 8B). The folds have variable orientations (Fig. 3) and in some cases were refolded due to progressive deformation during continued movement of the lava. A zone of flow breccia occupies the uppermost 50 m of the flow and consists of chaotically arranged, flow-banded rhyolite clasts as much as 1.5 m across (Fig. 8C). This breccia grades into the underlying coherent lava across a transitional zone in which flow-banded rhyolite shows incipient brecciation (Fig. 8D).

Bedded rhyolitic volcaniclastic rocks

The flow breccia at the top of the lower rhyolite flow is overlain by a bedded rhyolitic volcaniclastic sequence 60 m thick (Figs. 3 and 9). Planar-laminated, siliceous vitric tuff, crystal-vitric tuff, and tuffaceous mudstone containing quartz crystals ≤0.5 mm across make up most of the sequence (Figs. 10A and 10B). Some of the laminae are outlined by thin zones of secondary silicification that form thin, discontinuous, lenticular masses parallel to the lamination (Fig. 10C). Poorly preserved bubble-wall shards are visible in thin section but have been variably overprinted by growth of secondary silica (Fig. 10D).

Two zones of intense soft-sediment deformation occur within the tuffaceous rocks and contain chaotically arranged, disharmonic, meter-scale soft-sediment folds that deform the lamination and range from upright to recumbent (Figs. 9 and 11A). A covered interval occurs above this part of the sequence but is most likely underlain by similar tuffaceous rocks. It is succeeded by a 2.7-m-thick, planar, ledge-forming, massively bedded conglomerate containing well-rounded cobbles and boulders of aphyric rhyolite as much as 40 cm long. These clasts do not resemble the lower rhyolite flow and were presumably derived from another flow unit. The

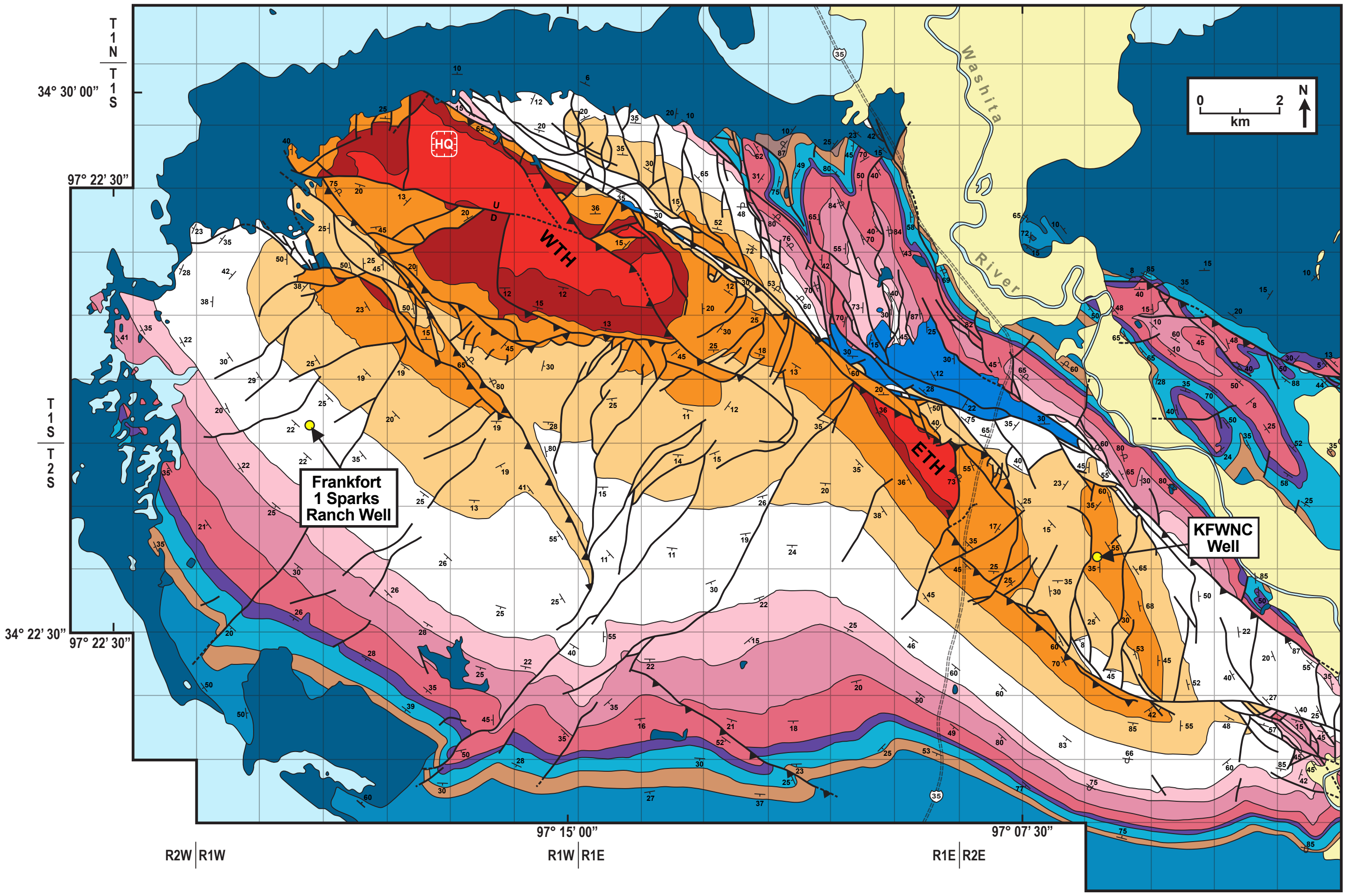

Figure 2. Geologic map of the western Arbuckle Mountains, including the West Timbered Hills (WTH) and the East Timbered Hills (ETH). Modified from Johnson (1990). Locations of Kaiser Francis-Westheimer Neustadt 1 Chapman (KFWNC) well and Frankfort 1 Sparks Ranch well are indicated. HQ: Hanson Aggregates Quarry. Legend for map is shown on the next page.

conglomerate is very poorly sorted, with a silt- and sand-sized matrix between the coarser clasts, and is generally massively bedded, except for diffuse stratification defined by thin mudstone laminae in the upper 5 cm of the unit.

The conglomerate is overlain by a 30-cm-thick unit consisting of massively bedded rhyolitic lapilli tuff grading upward into very fine grained tuff. Small pumice clasts a few millimeters long show flattening due to burial compaction (cf., Bull and McPhie, 2007). The rest of the sequence above this unit consists of beds of rhyolite pebble conglomerate and sandstone ~1 m thick (shown schematically in Figure 9) intercalated with beds of planar-bedded vitric tuff, mudstone, and siltstone as much as 20 cm thick. The conglomerates are matrix supported, massively bedded, and contain subangular to angular rhyolite clasts as much as 6 cm long.

Several faults with variable trends offset the bedded volcaniclastic rocks, which are completely faulted out against the upper rhyolite flow to the north and south (Fig. 3). The complex geometry of these faults is only partly understood because critical parts of the area are heavily vegetated. The conglomerates present in the upper part of the measured section (Fig. 9) do not occur in the other faulted segments of the bedded volcaniclastic rocks, suggesting that they may occupy a channel eroded into the tuffaceous rocks.

Upper rhyolite flow

The upper rhyolite flow can be traced for 3.5 km along strike before being truncated by thrust faults to the north and east. The exposed thickness of the flow is ~600 m, but

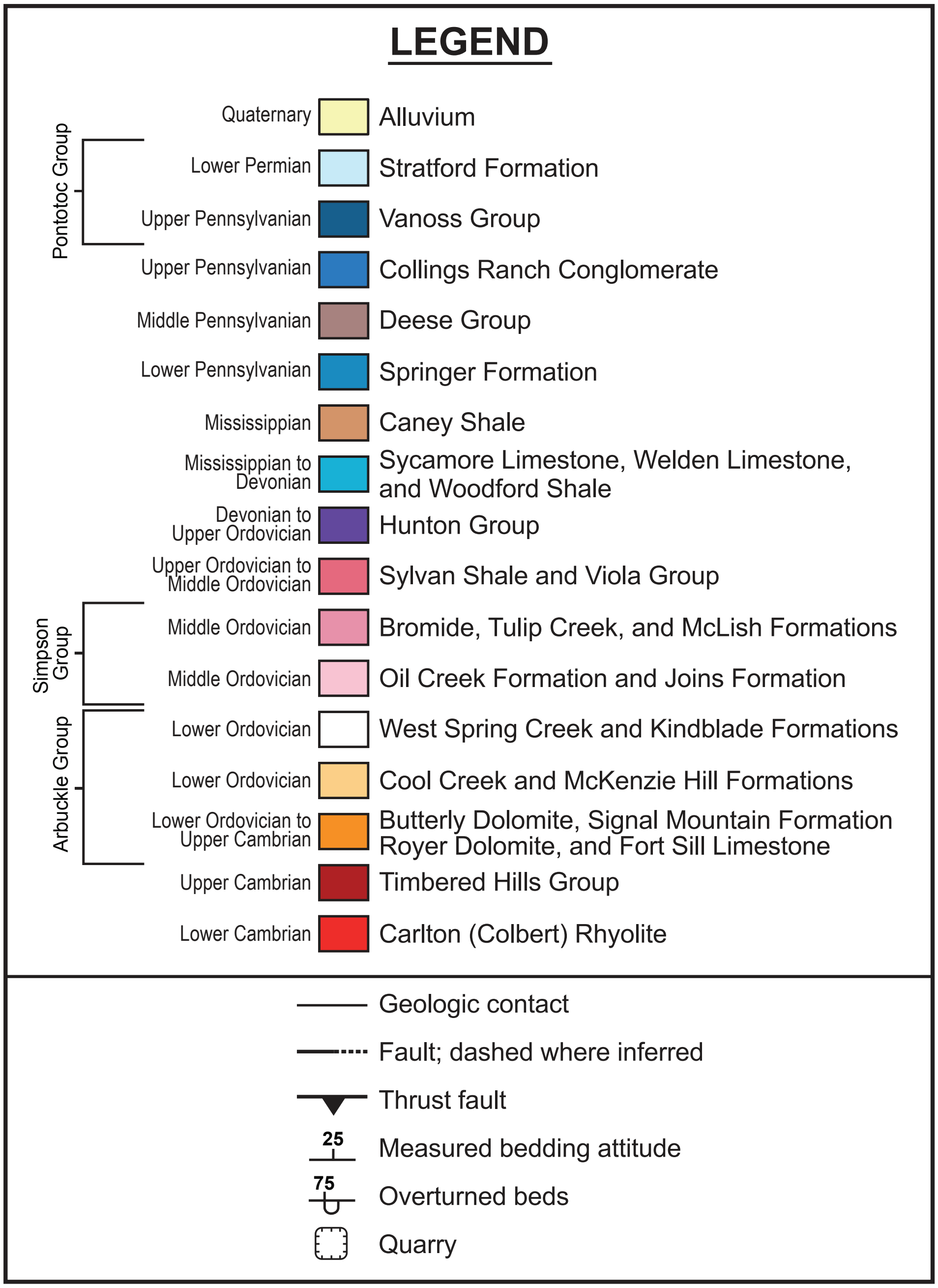

Figure 2 continued. Legend for geologic map of the western Arbuckle Mountains.

this is a minimum value because some of the upper parts were undoubtedly eroded away prior to deposition of the unconformably overlying Reagan Sandstone. In contrast to the lower rhyolite flow, the upper flow contains abundant phenocrysts and exhibits a regular vertical variation in groundmass textures (Fig. 4).

The groundmass in the lower 40 cm of the flow is generally dark-gray to black and records rapid chilling to glass, which was subsequently altered to iron-rich clays. Delicate flow lamination is well developed in this zone (Fig. 11B) but becomes less pervasive upward and typically disappears within a few meters of the basal contact. Quartz-filled amygdules aligned parallel to the flow lamination are present in minor amounts (Fig. 11C). Thin spherulitic layers developed along some flow laminae during initial high-temperature devitrification, and spherulites also nucleated on xenoliths of tuffaceous sediment derived from the underlying bedded volcaniclastic sediments (Fig. 11C). Discontinuous pockets of peperite ≤10 cm thick formed at the base of the flow by quenching and fragmentation of rhyolite lava and intermixing with wet, unconsolidated tuffaceous sediments at the top of the bedded volcaniclastic sequence. Dark-colored, blocky rhyolite fragments in the peperite are separated by disrupted tuffaceous mudstone, and some rhyolite fragments show jigsaw texture resulting from nonexplosive, in situ quench fragmentation (Figs. 12A and 12B).

The basal glassy zone passes upward into a zone ~40 m thick in which the groundmass has a heterogeneous appearance in hand sample, with abundant small, white spherulites ≤0.5 mm in diameter dispersed in pink-gray, holocrystalline rhyolite (Fig. 12C). Above this zone, homogeneous, red-gray felsitic rhyolite (Fig. 12D) forms a zone as much as 100 m thick in the slowly cooled interior of the flow. This zone passes upward into an upper heterogeneous, spherulitic zone that generally extends to the unconformity against the Reagan Sandstone. However, in one area ~90 m across in the uppermost exposed part of the flow (Fig. 3), the groundmass has the same dark-gray to black color as does the altered glass at the base of the flow. This uppermost glassy zone suggests the unconformity surface is close to the original top of the flow, at least in this part of the study area.

Although flow lamination or banding is generally absent above the glassy zone at the base of the flow, subtle flow lamination defined by aligned Fe-Ti oxide microlites

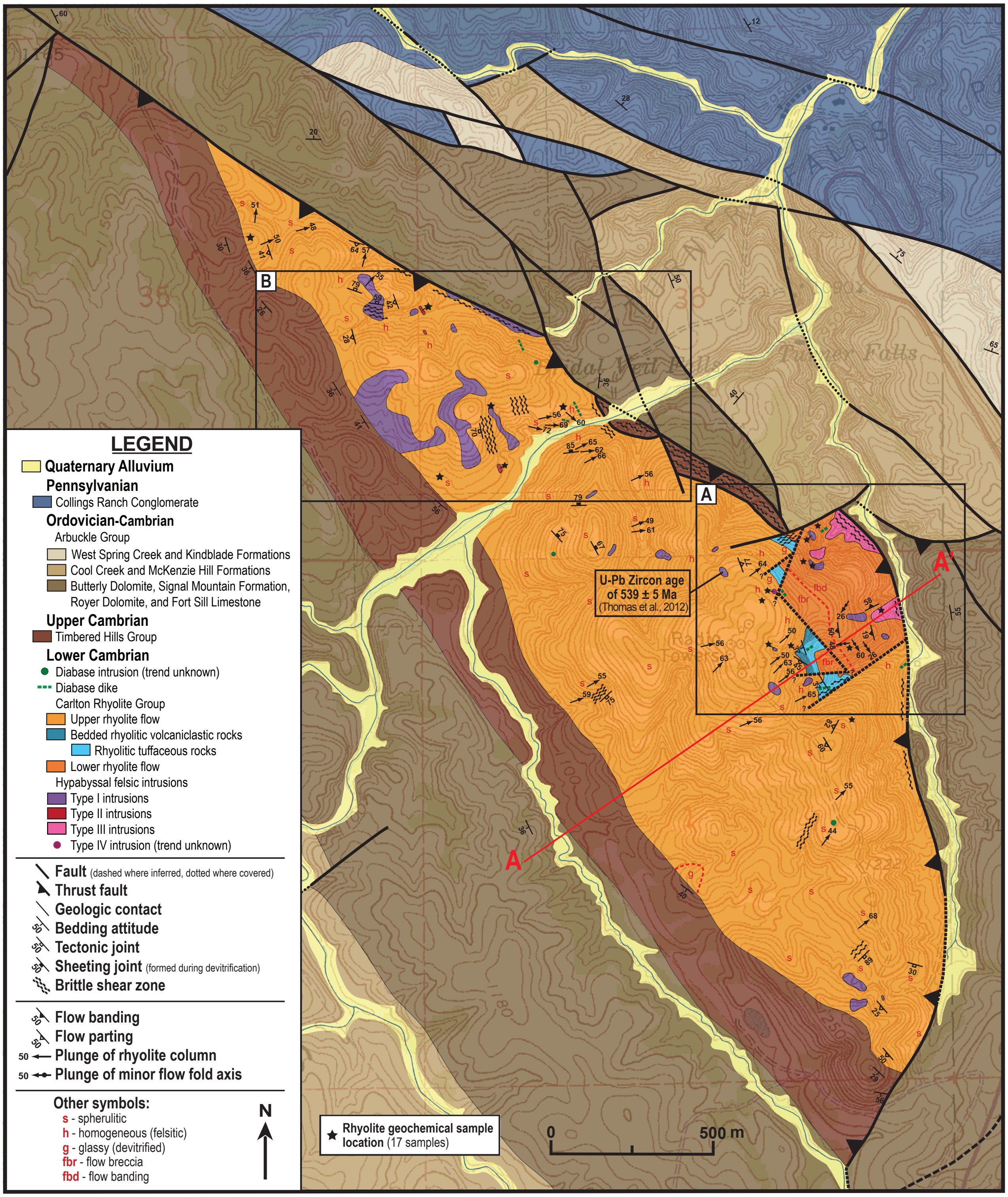

Figure 3. Geologic map of the East Timbered Hills. Panels A and B show closer views of part of map area. Red dashed lines indicate boundaries between originally glassy and heterogeneous, spherulitic zones near top of upper rhyolite flow and between flow-brecciated and flow-banded parts of lower rhyolite flow. Line A-A' indicates location of cross section shown in Figure 4. Location of measured section shown in Figure 9 is also indicated. Geology of Upper Cambrian−Quaternary units is modified from Johnson (1990).

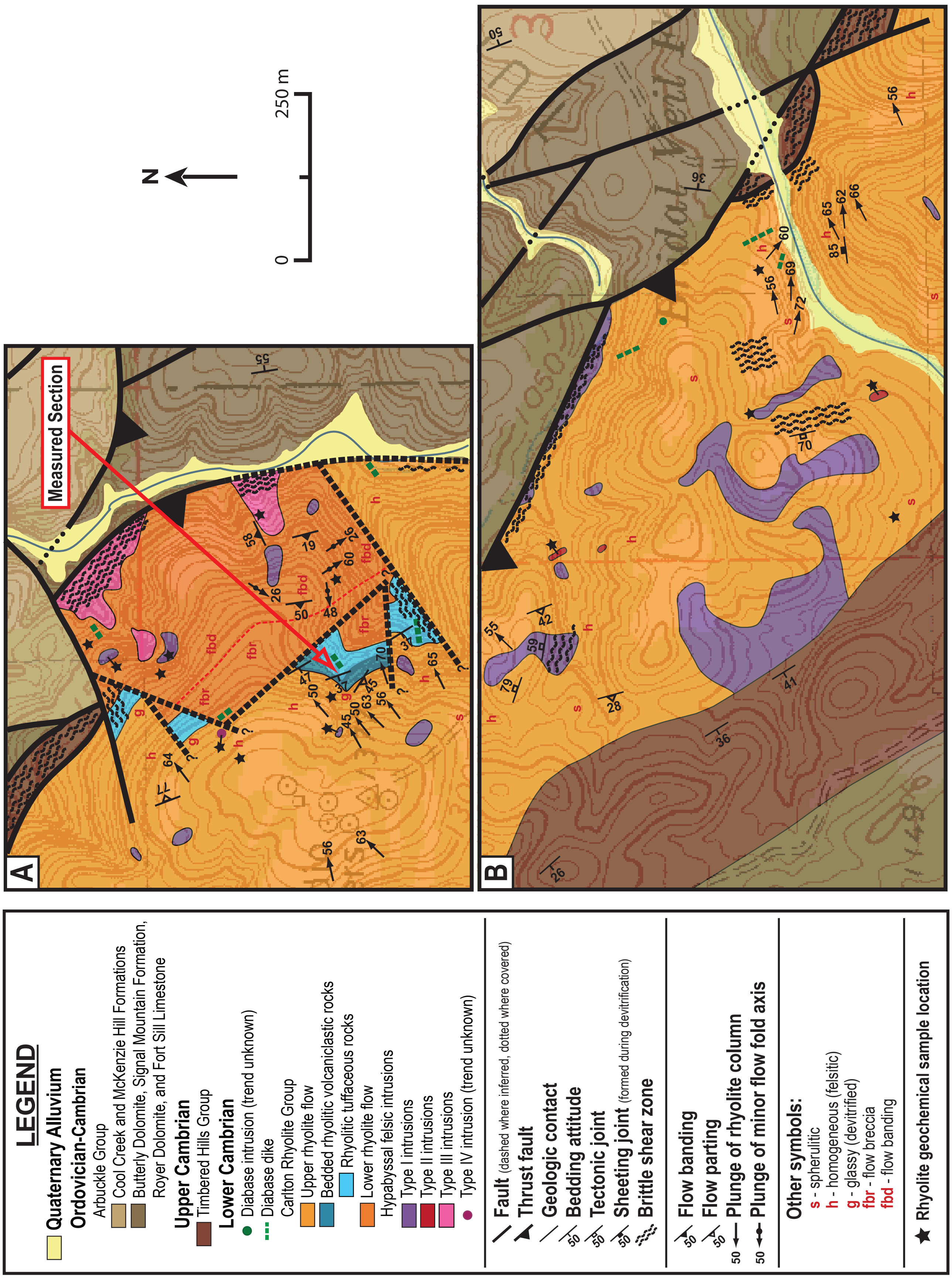

Figure 3 continued.

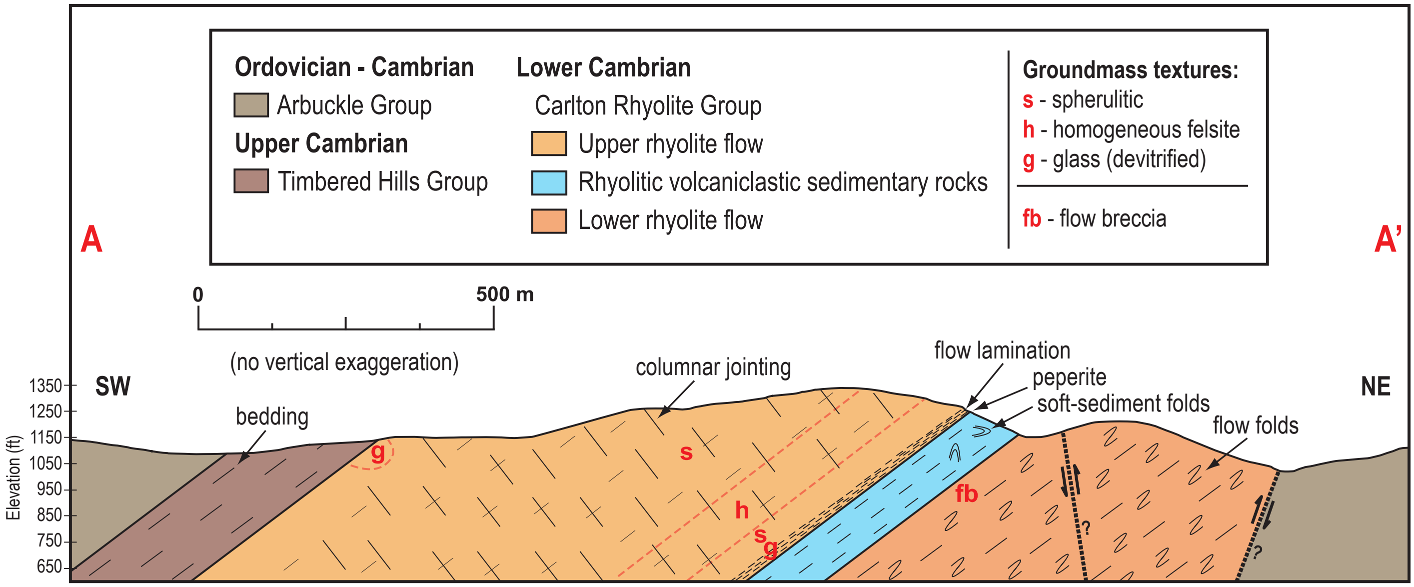

Figure 4. Cross section of East Timbered Hills; location is shown in Figure 3. Hypabyssal felsic intrusions are not shown because their three-dimensional geometries are unknown. Boundaries between different textural zones in groundmass of upper rhyolite flow are shown schematically by orange dashed lines.

occurs in some thin sections of the interior felsitic zone. Flow parting occurs in places throughout the flow and is defined by variably developed, closely spaced (≤4 cm), parallel planar surfaces. These surfaces are typically approximately parallel to the base of the flow, the orientation of which is constrained by bedding attitudes in the underlying bedded volcaniclastic sequence (Fig. 13). Bedding in the Reagan Sandstone above the upper flow has similar orientations to the flow parting within the flow (Fig. 13), suggesting there is relatively little angular discordance across the unconformity.

Columnar jointing is generally uniformly developed throughout the upper flow (Fig. 14A). The columns are as much as 1 m wide and many have hexagonal cross sections (Fig. 14B). They typically plunge steeply (50º to 70º) to the northeast, approximately perpendicular to the base of the flow (Fig. 13). Sheeting joints of the type described in Hanson et al. (this guidebook) and inferred to record volume decrease during devitrification overprint the columns to varying degrees (Fig. 14C).

Modal analyses of the upper flow are given in Table 1. Feldspar phenocrysts range in abundance from ~24 to 34 %. They are dominantly alkali feldspar, although some plagioclase phenocrysts are also present. All of the feldspars show variable alteration to sericite, and some are replaced by chessboard albite. The alteration makes it difficult to distinguish alkali feldspar from plagioclase, and they were grouped together during point counting. Quartz phenocrysts (Fig. 15A) range in abundance from ~1.0 to 10 %, and titanomagnetite and mafic silicate phenocrysts together make up ~4 to 13 %. Primary titanomagnetite is partly altered to hematite and leucoxene, and the mafic silicates have been completely replaced by green clay (Fig. 15B), magnetite, hematite, and, in some cases, fluorite. Based on crystal shapes, most of the mafic silicate phenocrysts appear to have been pyroxene and possibly fayalite. Minor amounts of pseudomorphs after biotite also occur in a few samples. Trace amounts of apatite and zircon are typically present. Glomeroporphyritic texture is common, and some glomerocrysts consist of as many as 15 or more interlocking crystals. Feldspar is the main component in the glomerocrysts (Fig. 15C), although titanomagnetite, mafic silicate pseudomorphs (Fig. 15B), quartz, and very fine grained apatite and zircon may also be present.

In thin section the groundmass in the homogeneous, felsitic zone in the center of the flow contains very fine grained, subhedral to anhedral, intergrown quartz and feldspar and some small spherulites. A similar quartzo-feldspathic intergrowth occurs between the spherulites in the upper and lower zones that have a more heterogeneous appearance in hand sample, but the spherulites in these zones are more numerous than in the interior felsitic zone. Randomly oriented tridymite needles (now inverted to quartz) are common in the groundmass and increase in length from <0.01 mm near the margins of the flow to as much as 0.25 mm in the homogeneous, felsitic interior zone (Figs. 16A and 16B).

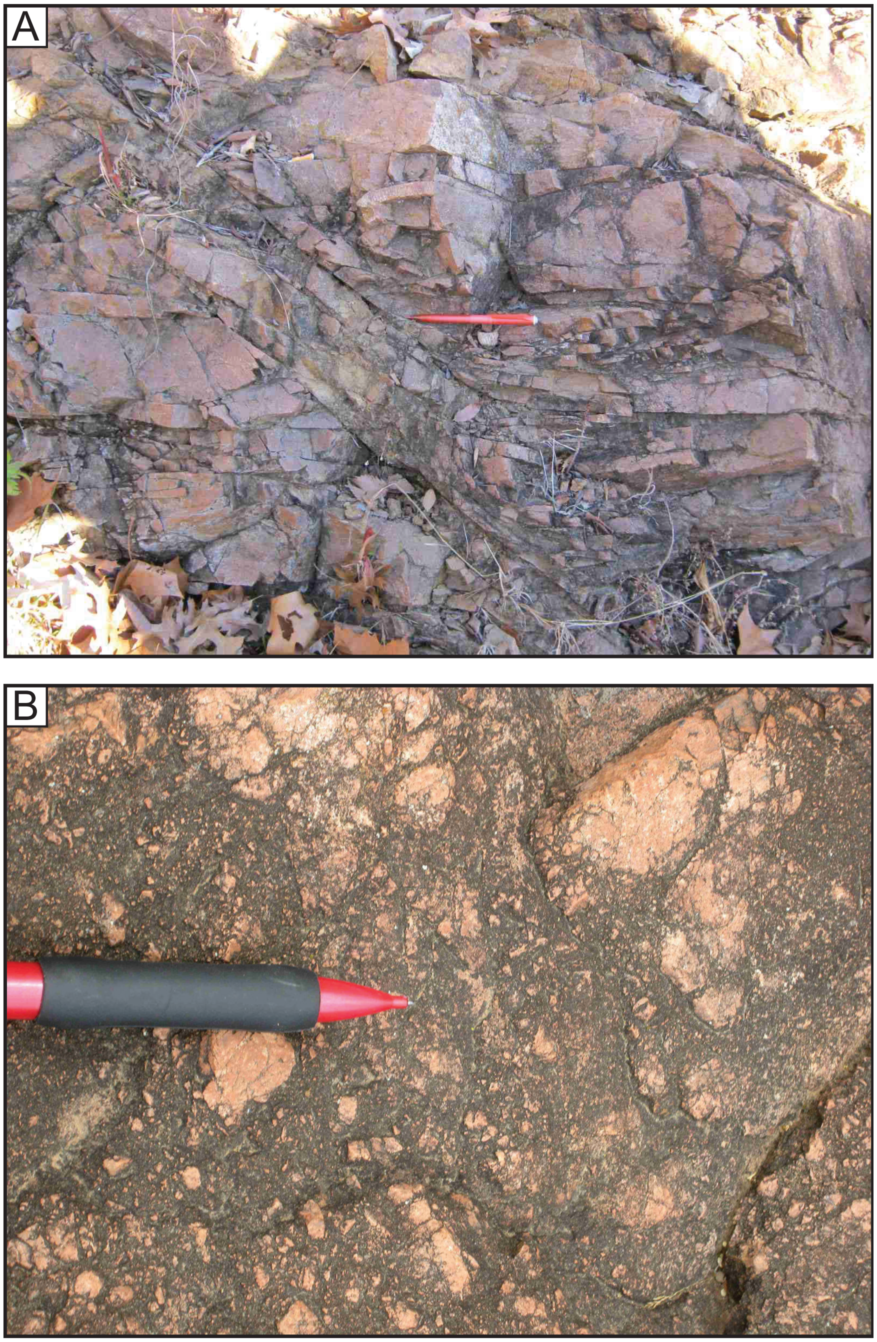

Figure 5. (A) Brittle shear zone in rhyolite flow; view is to northeast. (B) Fine-grained cataclasite in hypabyssal felsic intrusion.

Hypabyssal Felsic Intrusions

Four types of hypabyssal felsic rock intrude the two rhyolite flows in the ETH and can be distinguished based on phenocryst content and groundmass texture, as described below. The hypabyssal intrusions only rarely show columnar jointing or flow banding.

Type I Intrusions

Type I intrusions are the most abundant and are as much as 300 m across. Twenty separate Type I intrusions were mapped (Fig. 3), although they are probably at least partly interconnected in three dimensions. The U-Pb zircon age of 539 ± 5 Ma reported by Thomas et al. (2012) from the ETH comes from a small Type I intrusion within the upper flow (Fig. 3). The groundmass in the Type I intrusions has a distinctive orange-pink color in hand sample and varies from aphanitic to barely phaneritic, making these rocks transitional between hypabyssal rhyolite and microgranite. Alkali-feldspar and quartz phenocrysts are present (Table 1), and the latter occur as distinctive dipyramidal crystals as much as 3.5 mm across (Fig. 16C) that are larger and more abundant than in the upper rhyolite flow. The groundmass is characterized by well-developed microgranophyric texture (Fig. 16D). Sparse inclusions several millimeters across show coarser granophyric texture than is present in the host rock (Fig. 17A) and contain quartz phenocrysts. These inclusions are inferred to represent material that crystallized on the walls of the source magma chamber or conduit and was incorporated into the rising magma. Lithophysae as much as 1.5 cm across are present in one outcrop of the Type I intrusions, and small, irregularly shaped gas cavities ≤1 mm across are visible in thin section and are generally lined by drusy quartz crystals and filled with green clay (Fig. 16D). These features are consistent with intrusion at shallow levels, where volatiles could readily exsolve during cooling.

Type II Intrusions

Type II intrusions form three bodies as much as ~35 m across in the northwestern part of the study area. Quartz phenocrysts ~1 mm in length are very sparse, and the only other phenocrysts are mafic silicate crystals a few millimeters in length that are replaced by hematite and green clay; they were not point-counted because they are difficult to distinguish from alteration products in the groundmass. The aphanitic groundmass is orange-brown in hand sample and in thin

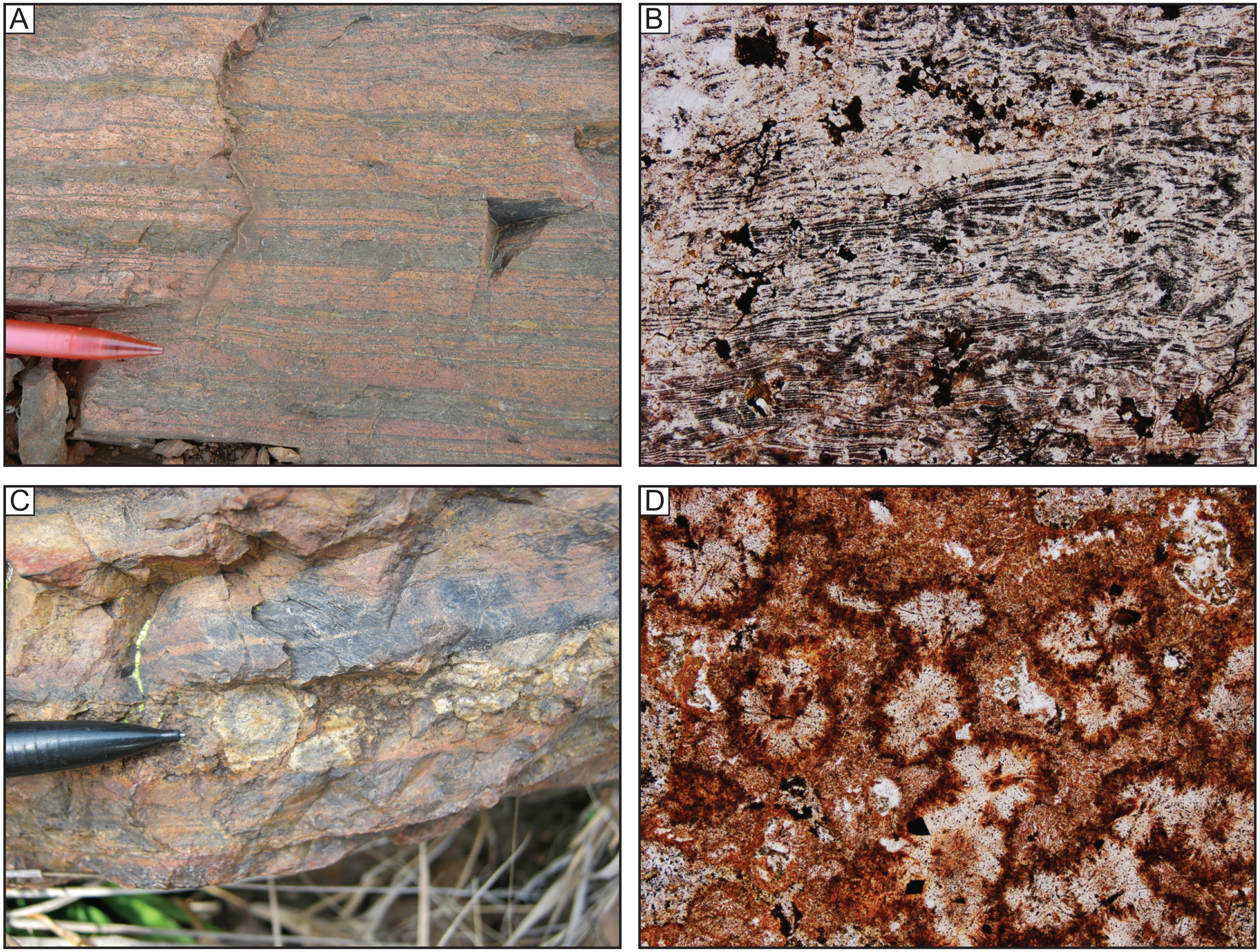

Figure 6. (A) Flow banding in lower rhyolite flow. (B) Photomicrograph of lower rhyolite flow showing flow lamination defined by opaque crystallites and overprinted by secondary silicification. Plane-polarized light; field of view ~2.5 mm across. (C) Spherulites in lower rhyolite flow showing concentric growth zones with different colors. (D) Photomicrograph of lower rhyolite flow showing densely coalescing spherulites. Plane-polarized light; field of view ~2.5 mm across.

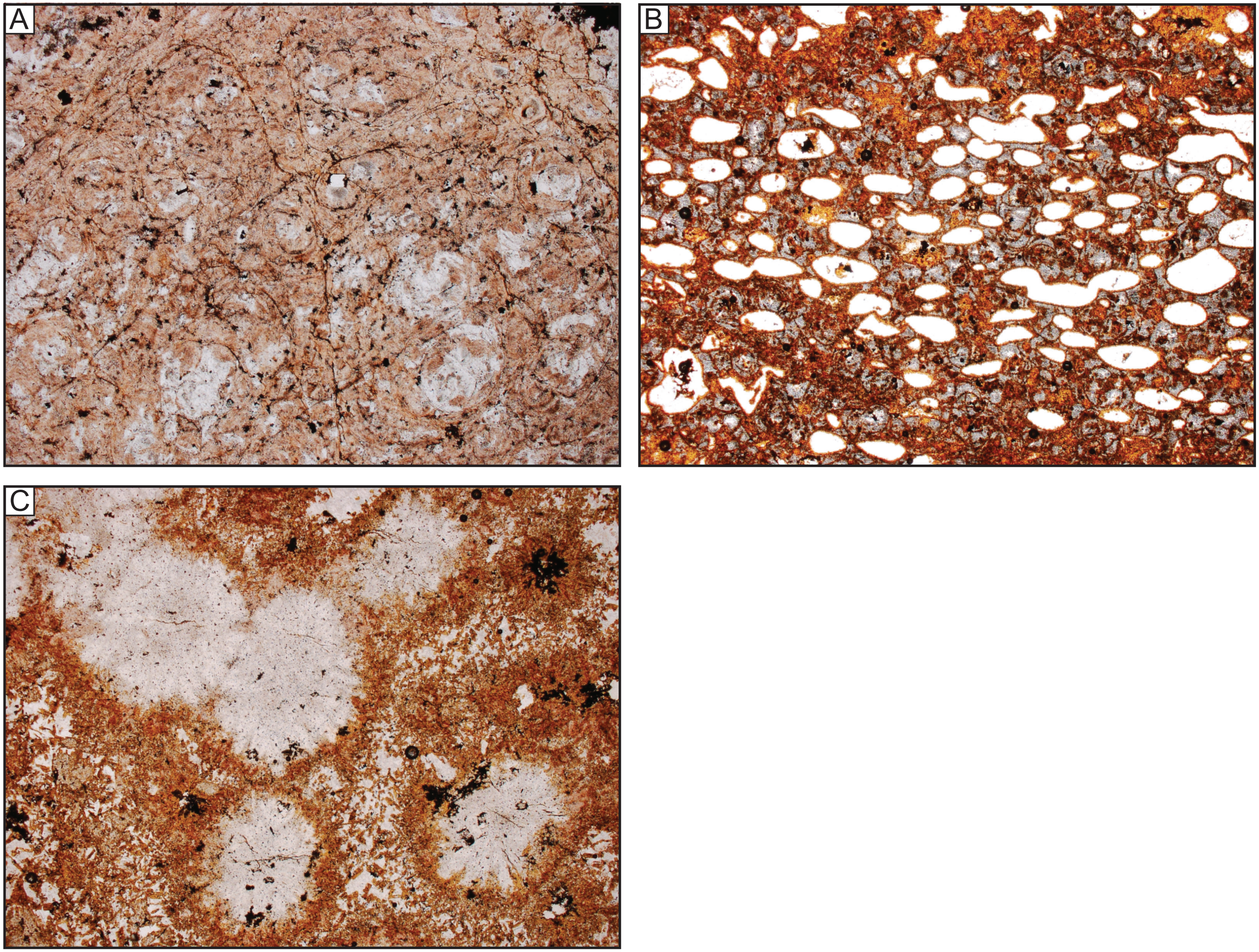

Figure 7. (A) Photomicrograph of lower rhyolite flow showing perlitic texture. Plane-polarized light; field of view ~5 mm across. (B) Photomicrograph of lower rhyolite flow showing vesicles (filled with quartz) oriented in direction of flow. Perlitic texture is visible in groundmass between vesicles. Plane-polarized light; field of view ~5 mm across. (C) Photomicrograph of lower rhyolite flow showing spherulites completely recrystallized to quartz. Plane-polarized light; field of view ~5 mm across.

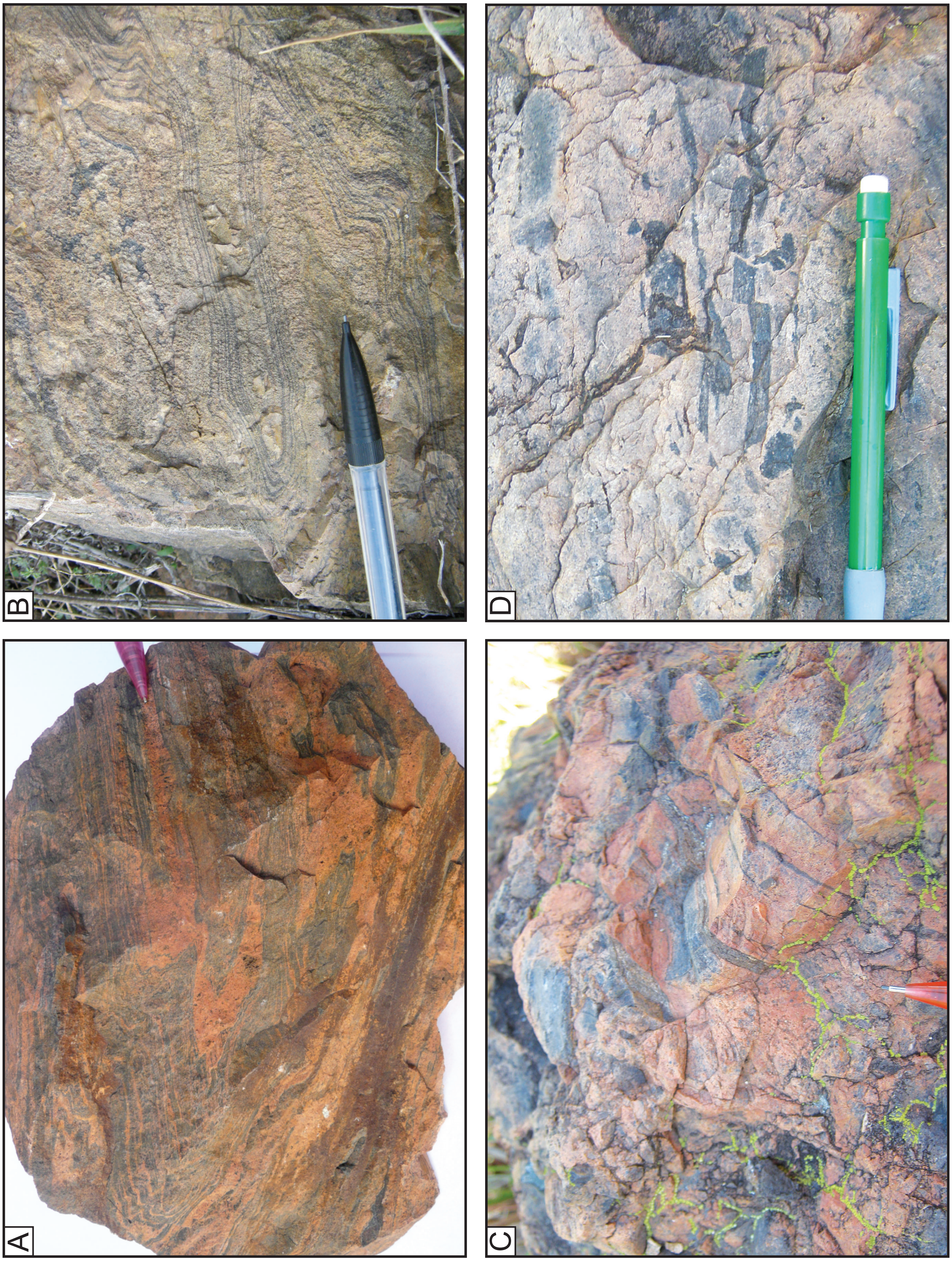

Figure 8. (A) Hand sample showing flow folds in lower rhyolite flow. (B) Outcrop view of flow folds in lower rhyolite flow. (C) Flow breccia in lower rhyolite flow. (D) Transitional zone between flow breccia and underlying lava in lower rhyolite flow showing incipient brecciation of flow bands.

section shows spherulitic texture grading into micrograno-phyre.

Type III Intrusions

Three Type III intrusions are present and are as much as ~180 m across, although the two larger ones are truncated by the Chapman Ranch Thrust Fault to the east (Fig. 3) and may have originally been considerably more extensive. They intrude only the lower rhyolite flow and are aphyric and typically pink-gray, except in zones of intense fracturing and cataclasis along the fault, where they are dark brick-red (Fig. 17B). The groundmass is barely phaneritic and in thin section exhibits spherulitic texture. Tridymite needles are as much as 1 mm in length, much longer than those in the upper rhyolite flow, and either are randomly oriented or radiate out from some of the spherulites (Fig. 17C). Interstitial, anhedral quartz and some micrograno-phyre are also present.

Type IV Intrusion

A single Type IV intrusion was mapped in the study area and was only found as locally derived float over a distance of ~2 m. Distribution of the float suggests that the intrusion may represent a poorly exposed dike. The unit is a pink-red rhyolite with alkali-feldspar phenocrysts as much as 2 mm across and well-developed spherulitic texture in the groundmass (Fig. 17D).

DIABASE INTRUSIONS

Seven steeply dipping diabase dikes as much as 2 m thick have been mapped in the study area and trend either northwest or northeast (Fig. 3 and Table 2). Three small diabase intrusions whose geometry and strike cannot be determined because of poor exposure are also shown in Figure 3, along with a larger intrusion exposed within rhyolitic tuffaceous rocks to the southeast of the towers on Signal Peak. That intrusion is at least 6 m wide and 12 m long. It may be a large dike but is extensively faulted, making its original geometry unclear. Most of the diabase intrusions were recognized based on locally derived, spheroidally weathered float, and additional intrusions almost certainly are present but are hard to identify in the more heavily vegetated parts of the study area.

The diabase intrusions occur within the lower and upper flows and the rhyolite tuff above the lower flow. None have been found in contact with the felsic hypabyssal intrusions, but this may simply reflect the sporadic occurrence of the diabases and their tendency to crop out poorly. Chilled tachylitic margins are visible in the better exposed dikes, and their interiors exhibit textures ranging from subophitic to locally ophitic in the coarser examples (Figs. 18A and 18B). Amygdules ≤1 mm in diameter are filled with green clay and minor epidote. Plagioclase shows variable alteration to sericite, which in many cases is nearly complete. Augite is generally less altered than plagioclase but is partly replaced by green clay + chlorite + actinolite ± goethite/hematite. Primary opaque minerals comprise titanomagnetite and small amounts of bladed ilmenite, and chlorite pseudomorphs of olivine occur in one sample (Fig. 18C).

FELSIC AND MAFIC ROCKS IN THE KFWNC WELL

A lithologic log for the KFWNC well is shown in Figure 19. The cumulative thickness of rhyolite penetrated in the well beneath strata of the Arbuckle and Timbered Hills Groups is 983 m. Thicknesses of individual units in the lithologic log are apparent thicknesses only, because the dip of the layers is unknown. The deeper parts of the well penetrated ~750 m of intrusive granite belonging to the Wich ita Granite Group before the Washita Valley Fault Zone was reached, and two granite intrusions interpreted to be sills also intrude parts of the rhyolite succession.

Fourteen different rhyolite flows have been distinguished in the well (Fig. 19) based on the general appearance of the cuttings under the binocular microscope and differences in phenocryst content and groundmass texture visible in thin section. The majority of the flows yield dark-reddish-brown to orange or reddish-orange cuttings which consist of felsitic rhyolite with spherulites and radiating to randomly oriented tridymite needles in the groundmass (Fig. 20A). Flow lamination is not present in cuttings from these intervals, which have similar groundmass textures to the upper rhyolite flow in the ETH. In contrast to that flow, however, quartz phenocrysts were not observed in any of the subsurface flows from these intervals, and alkali-feldspar and plagioclase phenocrysts typically either occur in sparse amounts or are absent. Flow 5 is the thickest flow and is 153 m thick; this flow also contains larger tridymite needles in the groundmass (as much 1 mm long; Fig. 20A) than are present in the other flows. Two intervals defined by dark-brown cuttings that in some cases show flow lamination occur between Flows 7 and 8 and Flows 8 and 9 and are interpreted to represent altered, originally glassy chilled margins to the flows (Fig. 19). In both cases, it is not known whether these intervals represent the chilled base of the overlying flow, the chilled top of the underlying

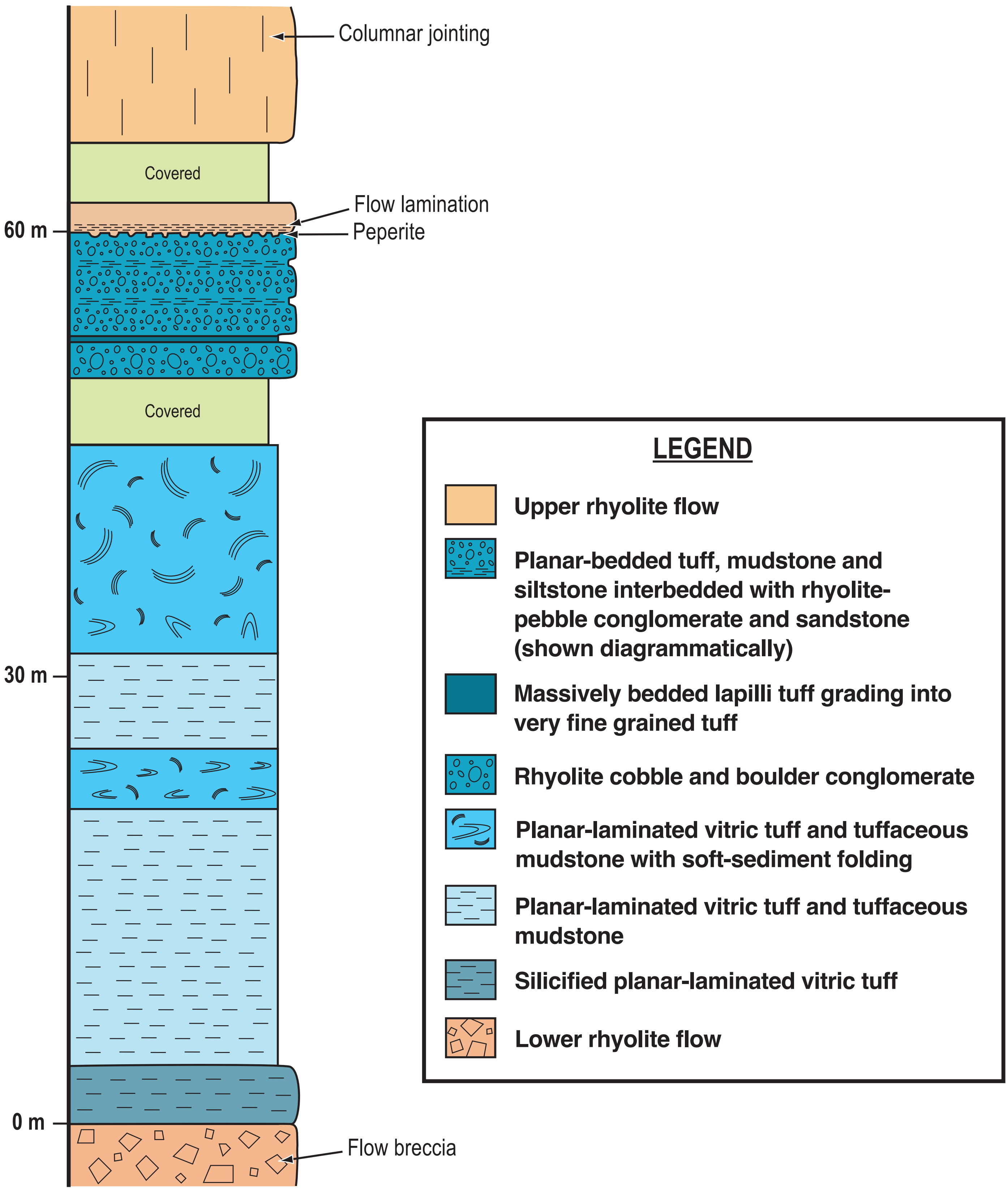

Figure 9. Measured section of bedded rhyolitic volcaniclastic sequence.

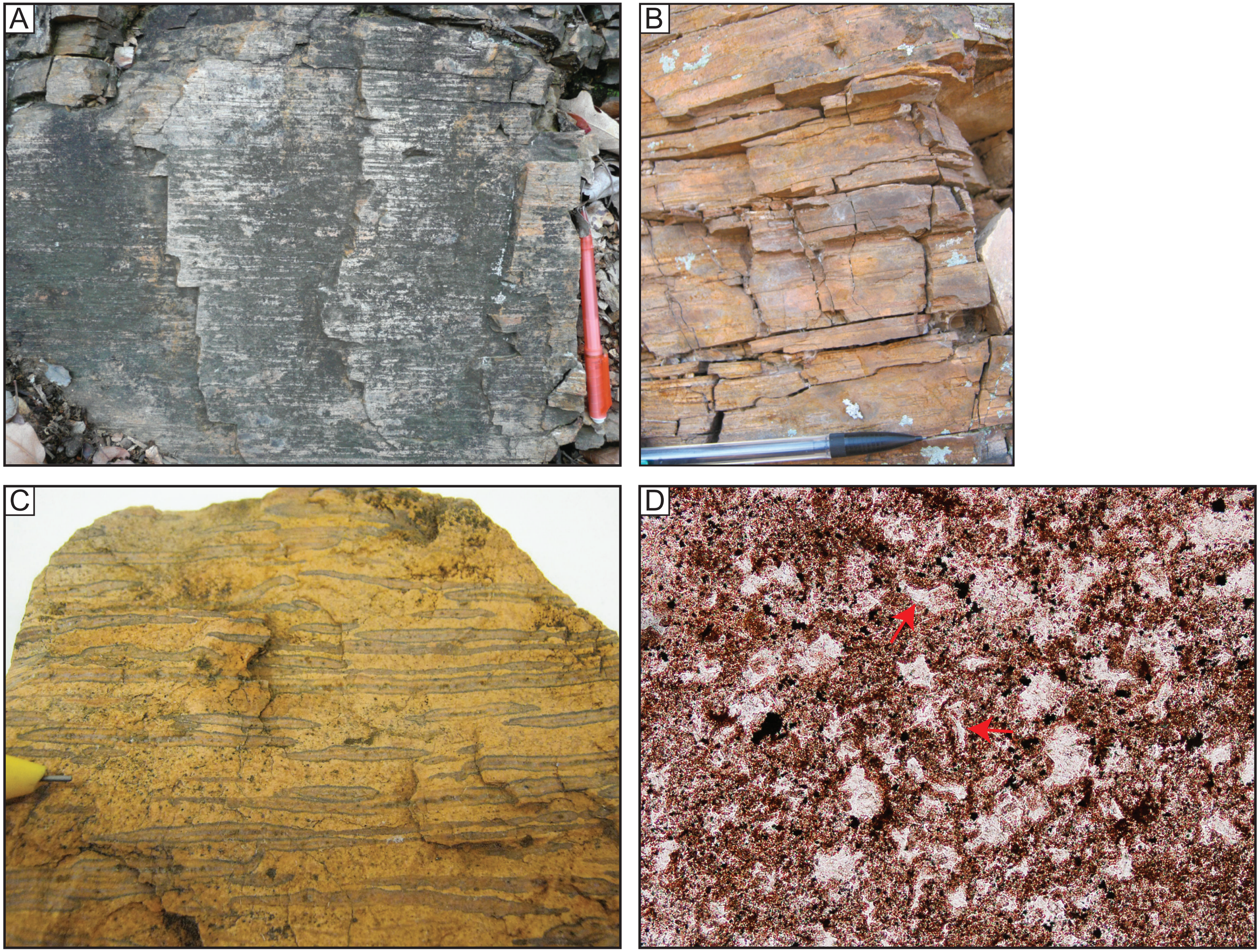

Figure 10. (A) Planar-laminated, very fine grained, siliceous vitric tuff in the bedded rhyolitic volcaniclastic sequence. (B) Closer view of planar lamination in siliceous vitric tuff. (C) Hand sample showing vitric tuff with laminae outlined by millimeter-scale zones of secondary silicification. (D) Photomicrograph of vitric tuff showing poorly preserved bubble-wall fragments overprinted by silicification; arrows point to examples. Plane-polarized light; field of view ~2.5 mm across.

TABLE 1: MODAL ANALYSES FOR EAST TIMBERED HILLS FELSIC ROCKS

Sample	Points Counted	Feldspar (%)	Quartz (%)	Mafic Silicate Pseudo-morphs (%)	All Dark-Colored Minerals Combined (%)	Titano-magnetite (%)	Ground-mass (%)	Maximum Feldspar Size (mm)	Maximum Quartz Size (mm)	Maximum Mafic Silicate Pseudomorph Size (mm)	Maximum Titanomag-netite Size (mm)	Maximum Glomerocryst Size (mm)
	slab/thin section	slab/thin section	slab/thin section	thin section	slab/thin section	thin section	slab/thin section					
Upper Rhyolite Flow												
277	1100/1440	28.7/–	0/1.0	3.5	12.8/–	3.0	58.5/63.8	7	1	1	0.6	6
281	1070/1430	27.2/–	0/2.0	2.6	4.0/–	3.0	68.6/65.2	7	0.75	1	0.6	7
282f	2160/1440	23.8/–	7.0/–	–	5.7/4.0	–	60.2/61.9	6	1	1	0.4	7
298	1600/1350	28.7/–	1.2/2.4	4.2	12.4/–	4.2	57.7/60.5	6	1	1.25	0.45	6
299	1450/1490	29.9/–	0.8/1.4	2.9	10.4/–	3.4	58.9/62.4	6	0.8	1	0.5	5
301	1860/1440	34.1/–	9.8/6.8	3.1	5.4/–	2.5	50.7/53.5	5	1	1.5	0.45	5
303	3050/1350	30.9/–	6.9/–	3.9	4.5/–	2.6	57.7/55.7	6	1	1.25	0.35	9
346	1264/1440	26.0/–	5.5/–	2.5	4.0/–	3.6	64.5/62.4	5	1.2	1	0.4	5
Type I Hypabyssal Felsic Intrusions												
279	1020/1440	8.0/8.4	14.3/–	–	12.7/9.2	–	65.0/68.1	5	3.5	4	–	6
286	1630/1440	15.2/8.4	14.5/–	–	9.8/11.9	–	60.5/65.2	4	2.5	1.5	–	6
320b	1940/1440	14.9/11.8	16.1/–	–	8.1/10.0	–	60.9/62.1	10	3.25	1.75	–	7

Number of points counted per sample for rock slabs was controlled by slab surface area, although the point interval was consistently 1 mm. Number of points counted per sample for thin sections was controlled by size and shape of the thin section, which varied slightly between samples, although the point interval was consistently 0.5 mm.

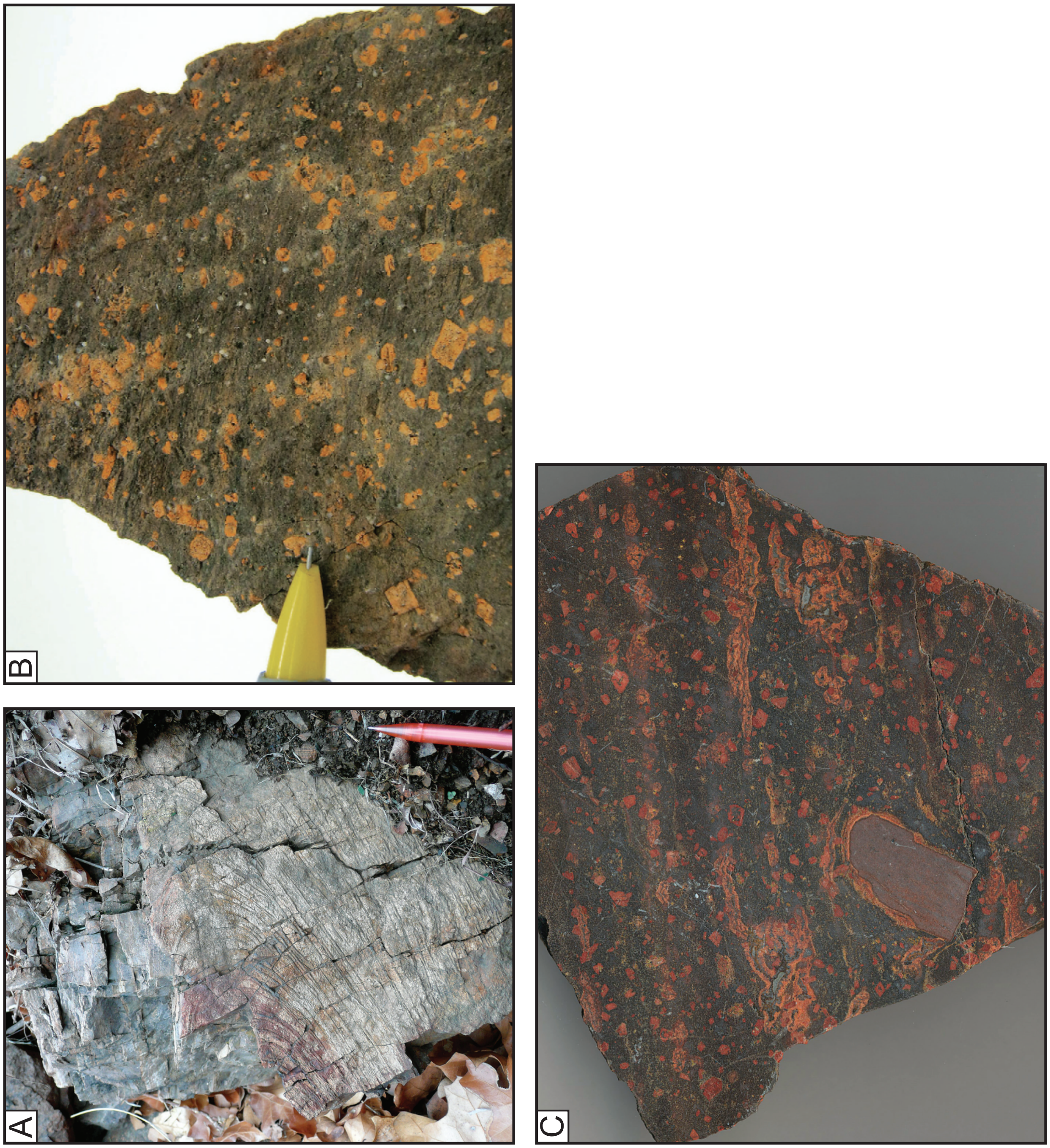

Figure 11. (A) Planar-laminated vitric tuff showing soft-sediment recumbent fold. (B) Hand sample from base of upper rhyolite flow showing dark gray to black groundmass and delicate flow lamination. (C) Sample from upper rhyolite flow above basal peperite zone. Sample contains a xenolith of tuffaceous sediment in lower left and shows a dark groundmass with flow lamination outlined by zones of spherulitic crystallization (pink-gray). Quartz-filled amygdules (white-gray) are also visible. Cut slab is ~16 cm across.

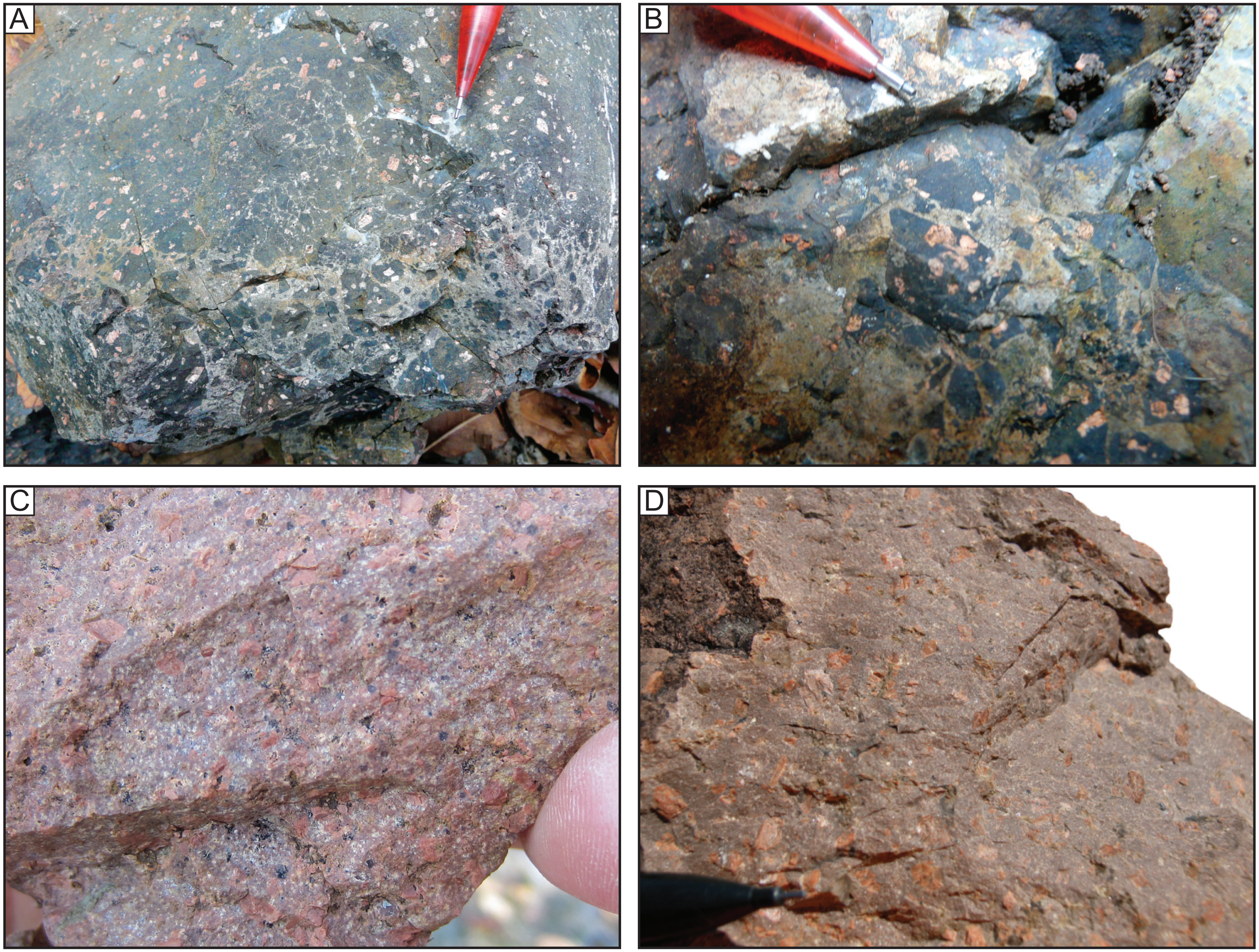

Figure 12. (A) Hand sample showing peperite at base of upper rhyolite flow. (B) Jigsaw texture in peperite zone at base of upper rhyolite flow. (C) Hand sample showing pink-gray heterogeneous spherulitic groundmass in upper rhyolite flow. Width of view ~3.5 mm across. (D) Hand sample showing red-gray homogeneous felsitic groundmass in interior of upper rhyolite flow. Tip of pencil for scale in lower left. Pink feldspar phenocrysts are visible in all photographs, and gray quartz phenocrysts are also visible in C and D.

flow, or a mixture of both.

Flow 2 is distinctly different from most of the other flows and is characterized by orange-gray cuttings in which the groundmass lacks tridymite needles and consists of very fine grained equidimensional quartz and feldspar containing small, dispersed spherulites (Fig. 20B). These textures overprint a delicate flow lamination (Fig. 20C) and are similar to those seen in parts of the lower rhyolite flow in ETH that initially remained glassy following emplacement. As in that flow, secondary quartz replaces the groundmass in small, irregular patches, making Flow 2 another example of an originally glassy flow that was susceptible to silicification.

Cuttings of Flow 3 lack flow lamination, but a similar very fine grained quartzo-feldspathic intergrowth to that in Flow 2 occurs in the groundmass (Fig. 20D), again indicating slow devitrification of originally glassy rhyolite. Flow 3 differs from Flow 2 and from the other flows in the well, however, because it contains relatively abundant quartz and feldspar phenocrysts, including chessboard albite (Fig. 20D). Flow 6 is underlain by an interval <3 m thick of rhyolitic volcaniclastic siltstone and sandstone, but this is the only volcaniclastic interbed recognized between flows in the succession penetrated by the well. Three intervals as much as 20 m thick are characterized by distinctive, orange-colored cuttings containing abundant quartz and alkali feldspar phenocrysts set in a groundmass showing well-developed micrographophyric texture (Fig. 21A). These units are similar to the Type 1 felsic intrusions present in the ETH and, like them, are inferred to represent hypabyssal intrusions within the rhyolitic volcanic pile.

A major part of Flow 10 is characterized by white to light-gray or tan cuttings with some thin granite veins. A thin section shows these cuttings to consist of rhyolite that has been almost completely recrystallized to granoblastic quartz and alkali feldspar by contact metamorphism against the underlying granite sill (Fig. 21B). Anhedral to subhedral andalusite is locally abundant in some cuttings and is intergrown with quartz (Fig. 21C). The presence of this aluminosilicate polymorph indicates that significant loss of alkalis occurred during metamorphism, creating an alumina-oversaturated composition. Similar metamorphic features occur in the Wichita Mountains in the Fort Sill area, where Carlton Rhyolite has been metamorphosed against Mt. Scott Granite (Finegan and Hanson, this guidebook). As in that example, Flow 10 was probably originally glassy, enabling nearly complete destruction of original volcanic textures during metamorphic recrystallization. One difference is that, in the Fort Sill area, sillimanite is also present, recording attainment of higher metamorphic temperatures in the contact metamorphic aureole of the thick Mt. Scott sill.

A number of mafic intrusions penetrate the rhyolites and granites (Fig. 19). Most of these are phaneritic diabases, but some of the thinner and more rapidly chilled ones are aphanitic basalt. We interpret a 13-m-thick basaltic unit between Flows 4 and 5 to represent a basalt lava flow interbedded with the rhyolites because it is unlikely that a mafic intrusion this thick would chill uniformly to basalt. The same conclusion applies to two other, thicker basaltic intervals intercalated with rhyolites in the lowest part of the rhyolite succession between ~1.49 and 1.54 km, above the large granite intrusion in the deepest parts of the well.

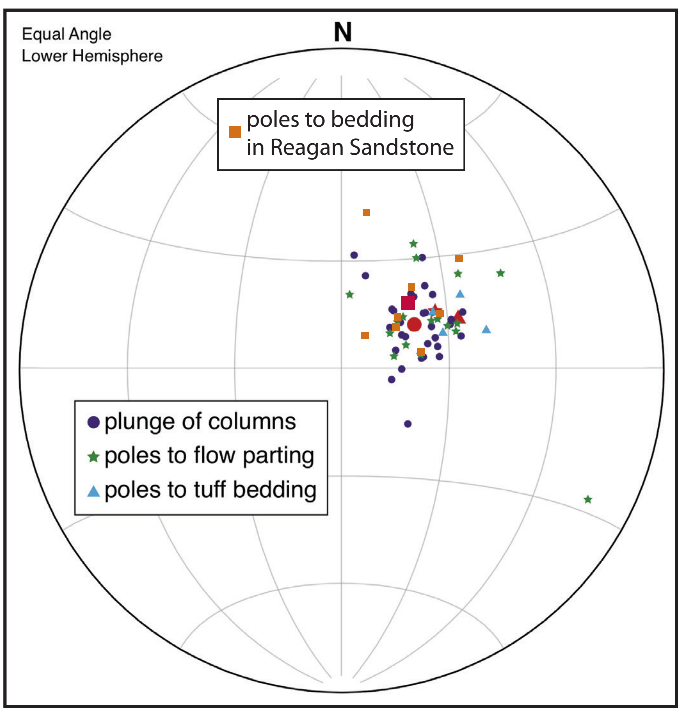

Figure 13. Stereonet showing plunge of column long axes, poles to flow parting in upper rhyolite flow, and poles to bedding in tuffaceous rocks and Reagan Sandstone. Larger red symbols with same shapes show mean poles.

GEOCHEMISTRY OF THE FELSIC ROCKS

Major elements

Major- and trace-element analyses for the felsic rocks are shown in Table 3, and the major oxides are plotted in Harker diagrams in Figure 22. The highest silica values, as much as 79.16 wt % (volatile-free), occur in the Type I intru-

Figure 14. (A) Columnar jointing in upper rhyolite flow; columns are ~1 m across. (B) Columnar jointing in upper rhyolite flow. Hammer rests on surface perpendicular to columns. (C) Sheeting jointing crossing columnar jointing in upper rhyolite flow.

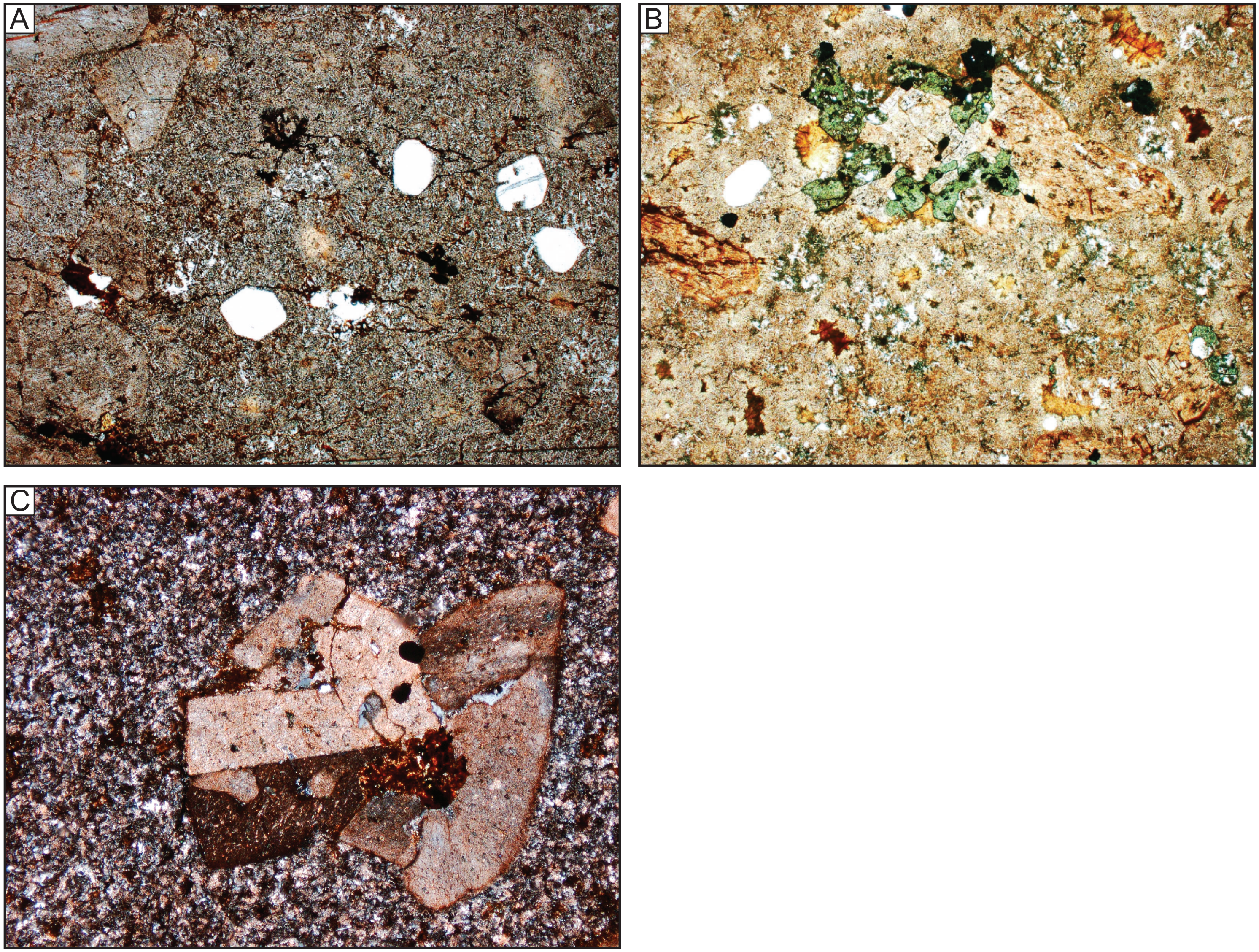

Figure 15. (A) Photomicrograph from upper rhyolite flow showing subhedral quartz phenocrysts with rounded corners; second phenocryst from right shows embayments. Feldspar phenocrysts are also visible. Plane-polarized light; field of view ~5 mm across. (B) Photomicrograph from upper rhyolite flow showing mafic silicate crystals completely replaced by green clay. Mafic silicates occur within a glomerocryst also containing feldspar and titanomagnetite crystals. Spherulites are visible in the groundmass. Plane-polarized light; field of view ~5 mm across. (C) Photomicrograph from upper rhyolite flow showing a glomerocryst consisting of crystals of plagioclase and alkali feldspar, mafic silicate pseudomorphs, and titanomagnetite. Crossed polars; field of view ~2.5 mm across.

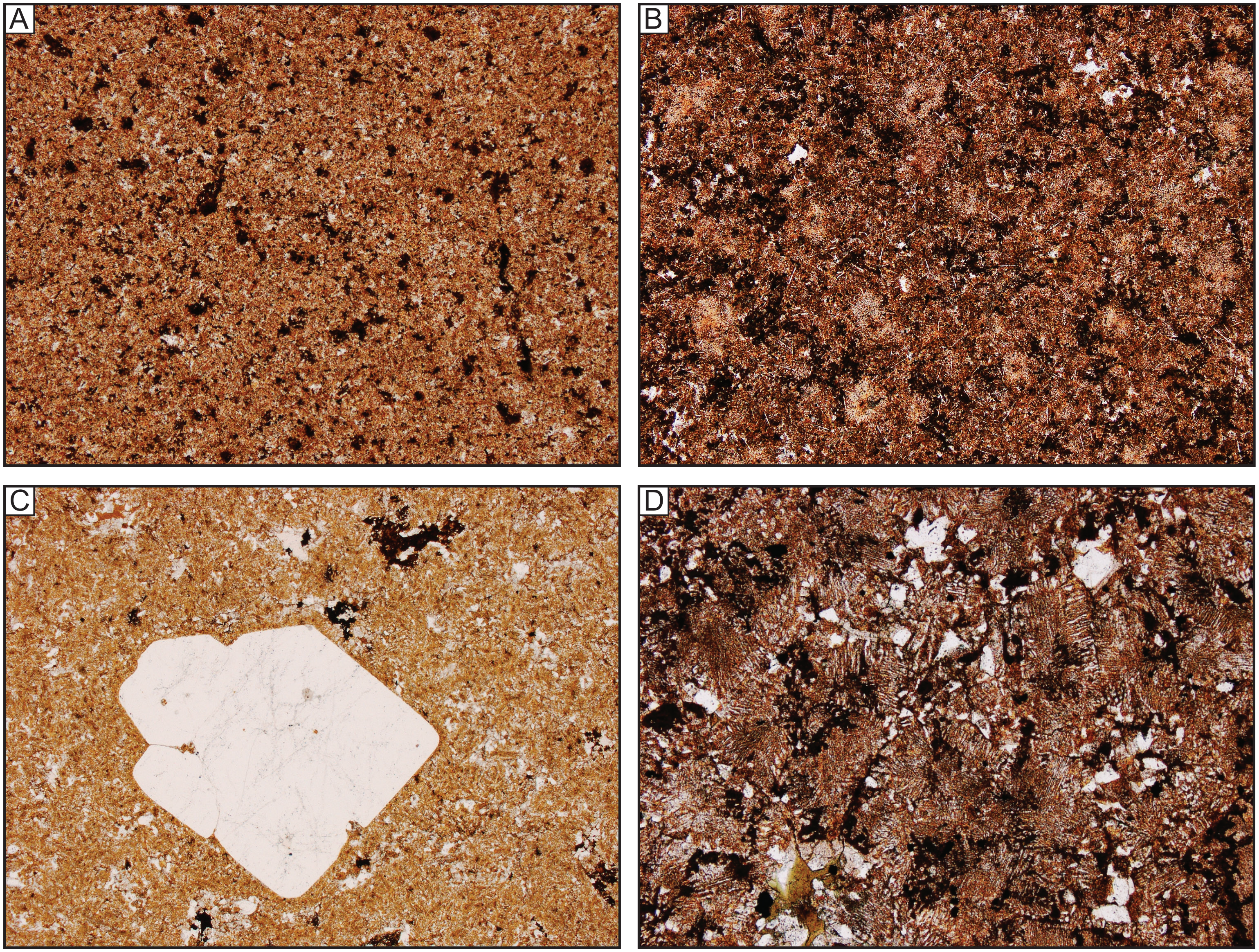

Figure 16. (A) Photomicrograph showing very fine grained tridymite needles (barely visible; now inverted to quartz) in groundmass near base of upper rhyolite flow. Plane-polarized light; field of view ~2.5 mm across. (B) Photomicrograph showing coarser tridymite needles in groundmass in interior of upper rhyolite flow. Spherulites are also visible. Plane-polarized light; field of view ~2.5 mm across. (C) Photomicrograph from Type I felsic intrusion showing dipyramidal quartz phenocryst. Plane-polarized light; field of view ~5 mm across. (D) Photomicrograph from Type I felsic intrusion showing well-developed micrograndophyric texture and an irregularly shaped gas cavity (at bottom left) filled with green clay and lined by quartz crystals. Plane-polarized light; field of view ~2.5 mm across.

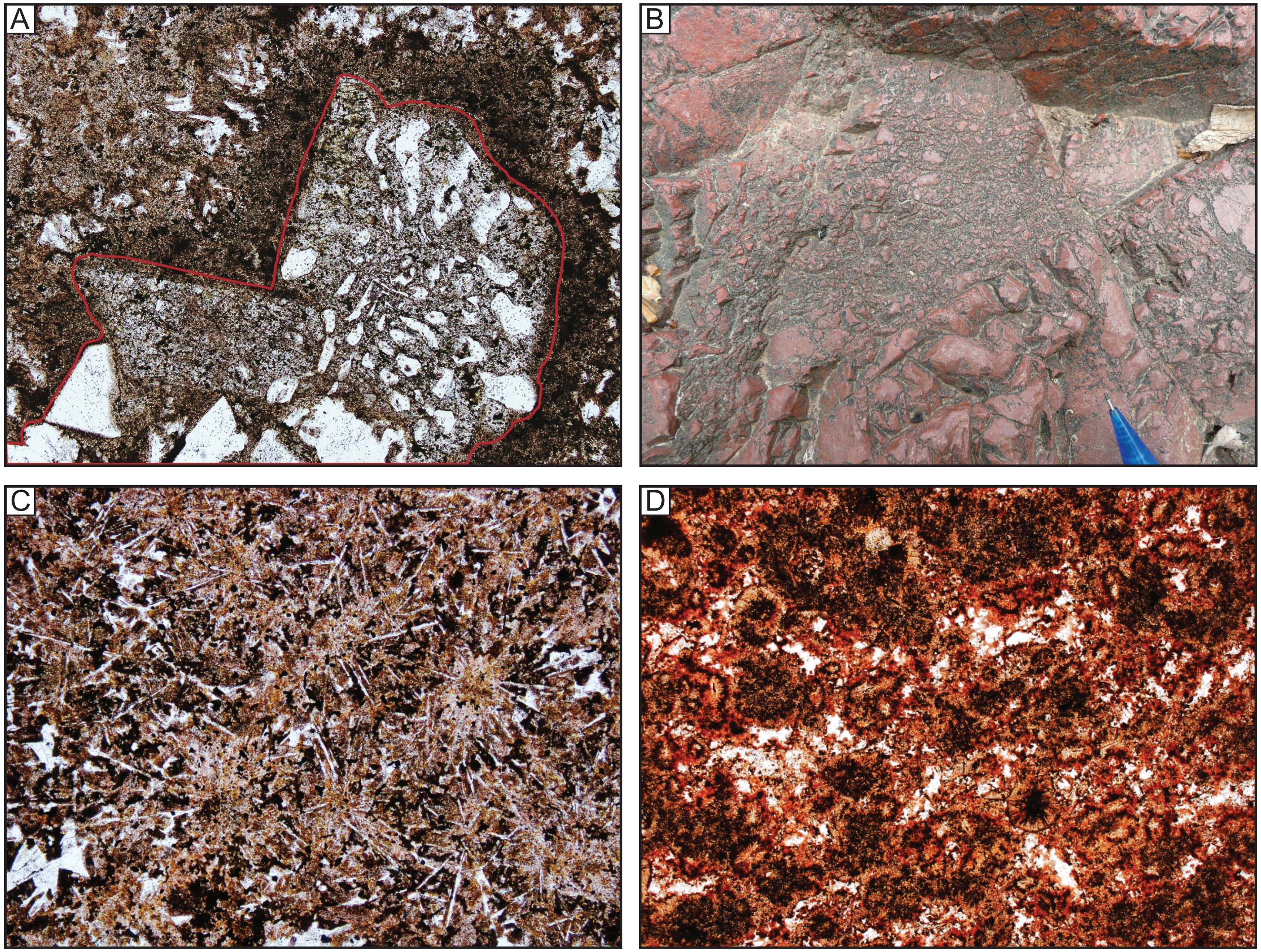

Figure 17. (A) Photomicrograph from Type I felsic intrusion showing a granophyric inclusion (outlined in red). Plane-polarized light; field of view ~2.5 mm across. (B) Stream-polished outcrop of Type III felsic intrusion showing zone of intense fracturing with local pockets of fine-grained cataclasite. (C) Photomicrograph from Type III felsic intrusion showing spherulites, coarse, randomly oriented tridymite needles, and anhedral, interstitial quartz. Plane-polarized light; field of view ~2.5 mm across. (D) Photomicrograph from Type IV felsic intrusion showing spherulitic texture. Plane-polarized light; field of view ~5 mm across.

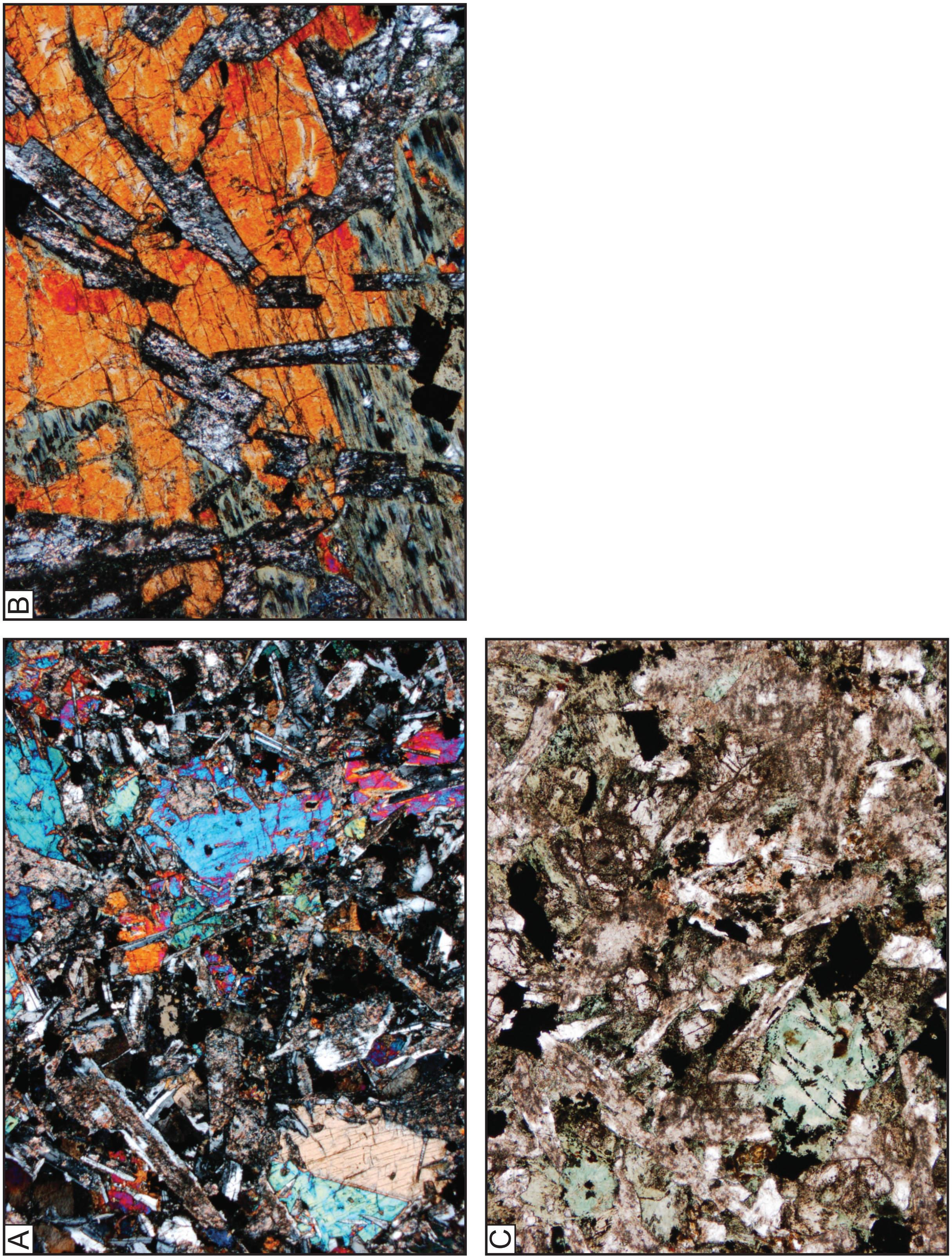

Figure 18. (A) Photomicrograph from diabase intrusion showing subophitic texture. Crossed polars; field of view ~5 mm across. (B) Photomicrograph from diabase intrusion showing local ophitic texture. Note highly altered plagioclase. Crossed polars; field of view ~2.5 mm across. (C) Photomicrograph from diabase intrusion showing chlorite pseudomorph of olivine in lower left with very fine grained iron oxide lining conchoidal fractures. Plane-polarized light; field of view ~2.5 mm across.

sions and are higher than typical silica contents for unaltered rhyolites. Type II intrusions also show relatively high silica values. However, there is no petrographic evidence for significant secondary silicification in either of these groups of intrusions, and their high silica contents are considered to be close to the primary values. Silica contents in the upper flow in the ETH range between 73.85 and 77.37 wt %, but petrographic evidence for significant secondary addition of silica in the samples with the higher silica contents is similarly lacking. Furthermore, the samples of this flow with the highest silica contents also have higher contents of quartz phenocrysts (Table 1). These observations indicate that the variable silica contents in the upper flow reflect primary compositional heterogeneities. On the other hand, the range in silica contents in the lower rhyolite flow (74.45 to 77.58 wt %) is at least partly the result of secondary silicification, as shown by the presence of silica veinlets in thin section as well as locally abundant quartz-filled vesicles (e.g., Fig. 7B).

Al_2O_3, CaO, TiO_2, and P_2O_5 show overall decreases with increasing silica (Fig. 22), consistent with fractionation of plagioclase, clinopyroxene, titanomagnetite, and apatite. In contrast, FeO and MgO are more scattered, which may be due partly to mobility of Fe and Mg during alteration of the primary mafic silicates. Na_2O decreases with increasing silica, whereas K_2O tends to show a slight increase. These trends should be interpreted with caution, however, because of the petrographic evidence for alkali mobility in these rocks (e.g., replacement of feldspar phenocrysts by chessboard albite and sericite). Several samples from the hypabyssal felsic intrusions plot to the right of the normal igneous spectrum in Figure 23, indicating addition of K_2O and loss of Na_2O during alteration. One anomalous sample from the lower rhyolite flow (sample 285; Table 3) that has very low Na_2O and unusually high K_2O is not shown in Figure 23 because it plots off the scale of the diagram. Only minor amounts of sericite occur in this sample, but its groundmass originally consisted entirely of glass, and disturbance of the alkalis may have occurred during devitrification. Comparable dramatic increases in the K_2O/Na_2O ratio have been shown to occur during devitrification of rhyolite glass by other workers (e.g., Simons, 1962).

TABLE 2. CHARACTERISTICS OF DIABASE DIKES IN EAST TIMBERED HILLS

Site Number	Estimated Trend (azimuth)	Thickness (m)	Exposed Length (m)
252	337°	1.0	12.0
274	050°	1.0	4.5
282a	330°	0.3	1.0
318	050°	2.0	9.0
352	055°	0.6	4.0
387	333°	1.0	12.0
388	285°	1.0	1.0

Trace elements

Because of the evidence for major-element mobility in some samples, trace elements susceptible to alteration must also be used with care in these rocks. For example, scatter in Rb and Ba in the Harker diagrams in Figure 24 is consistent with other evidence for alkali mobility in these rocks discussed above. The unusually low Ba contents in the Type I and Type II intrusions, however, are inferred to be a primary feature and are consistent with other evidence discussed below for the fractionated nature of these samples. Sc, which is fairly resistant to alteration (e.g., Rollinson, 1993), shows an overall negative correlation with silica (Fig. 24). This element is compatible in both pyroxene and titanomagnetite (Mahood and Hildreth, 1983; Bacon and Druitt, 1988; Rollinson, 1993), and its depletion with increasing silica most likely reflects fractionation of both these minerals. Sr also decreases with increasing silica (Fig. 24), consistent with feldspar fractionation.

Th, Zr, and Nb are typically immobile during low-temperature alteration (Pearce and Cann, 1973; Winchester and Floyd, 1977; Rollinson, 1993), but they do not show obvious trends in Harker diagrams when the data are considered as a whole (Fig. 24). In fact, the samples tend to plot in three main groups, except for the Type IV intrusion, which does not plot consistently with any of the groups. These three groups are best seen in the Harker diagrams for Nb and Th. One group includes the lower and upper rhyolite flows, the Type III intrusion from the ETH, and the rhyolite lava flows from the KFWNC well. The Type 1 and Type II intrusions plot separately in two other groups. Some of the variation between samples within these groups is due to silica mobility during alteration, but the three groups as a whole are considered to reflect primary compositional differences.

Because of the secondary alteration, standard rock classification schemes using major elements may not precisely classify the rocks. In such cases, the diagram of Winchester and Floyd (1977) (Fig. 25A) generally provides reliable results because it employs ratios of immobile trace elements (and TiO_2, which is also resistant to alteration). On this diagram, samples of the upper flow plot in the field for normal rhyolites, whereas samples of the lower flow, the Type I, II, and IV intrusions, and all but one of the rhyolite lavas in the KFWNC well fall in the peralkaline

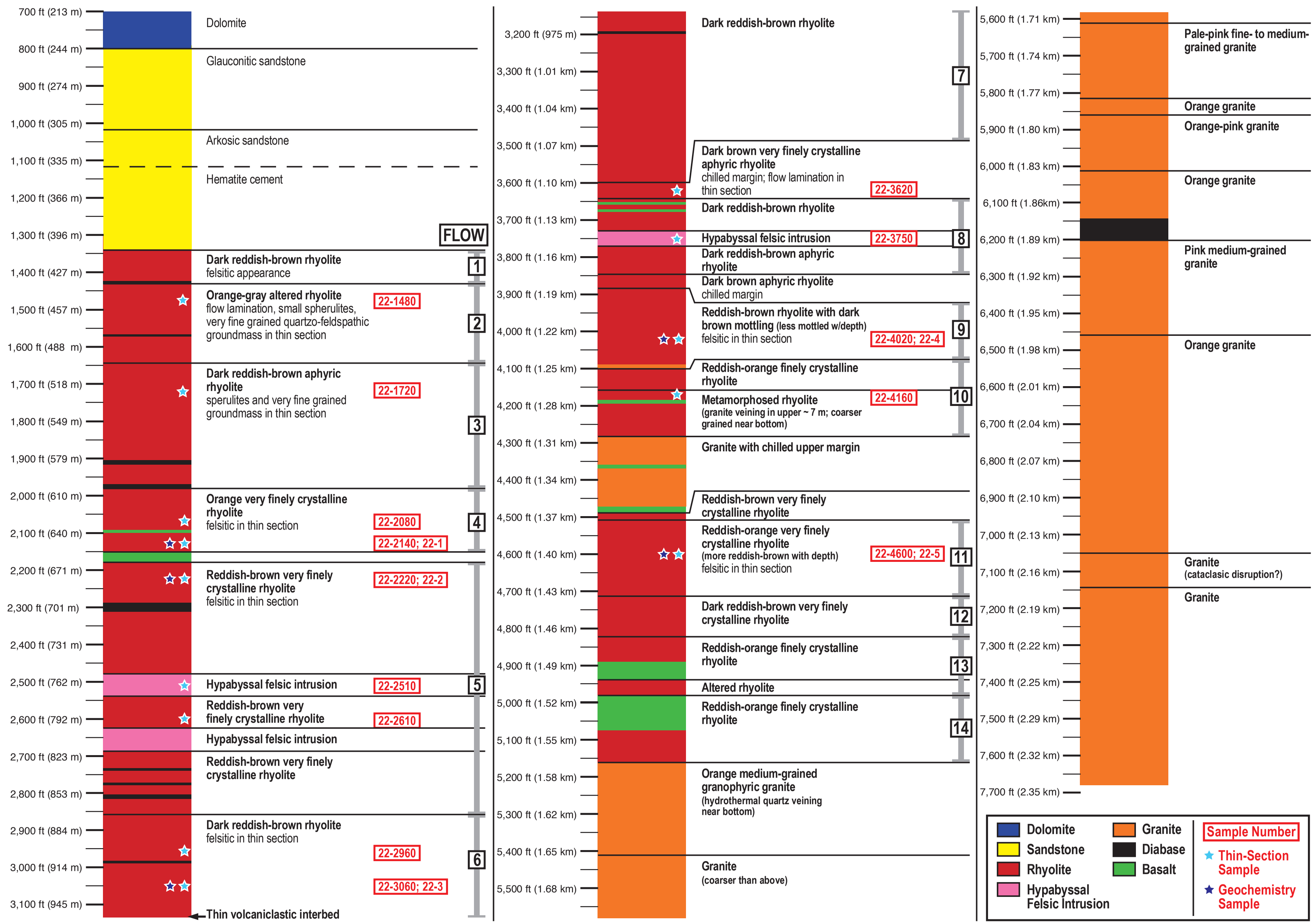

Figure 19. Lithologic log of Kaiser Francis-Westheimer Neustadt 1 Chapman (KFWNC) well based on study of drill-cutting samples taken at ~3 m intervals and correlated with gamma-ray logs. Locations of thin-section and geochemical samples are indicated on well log. Diabase or basalt intrusions <3 m thick are not shown to scale. Numbered rhyolite flow units are shown to the right of unit descriptions.

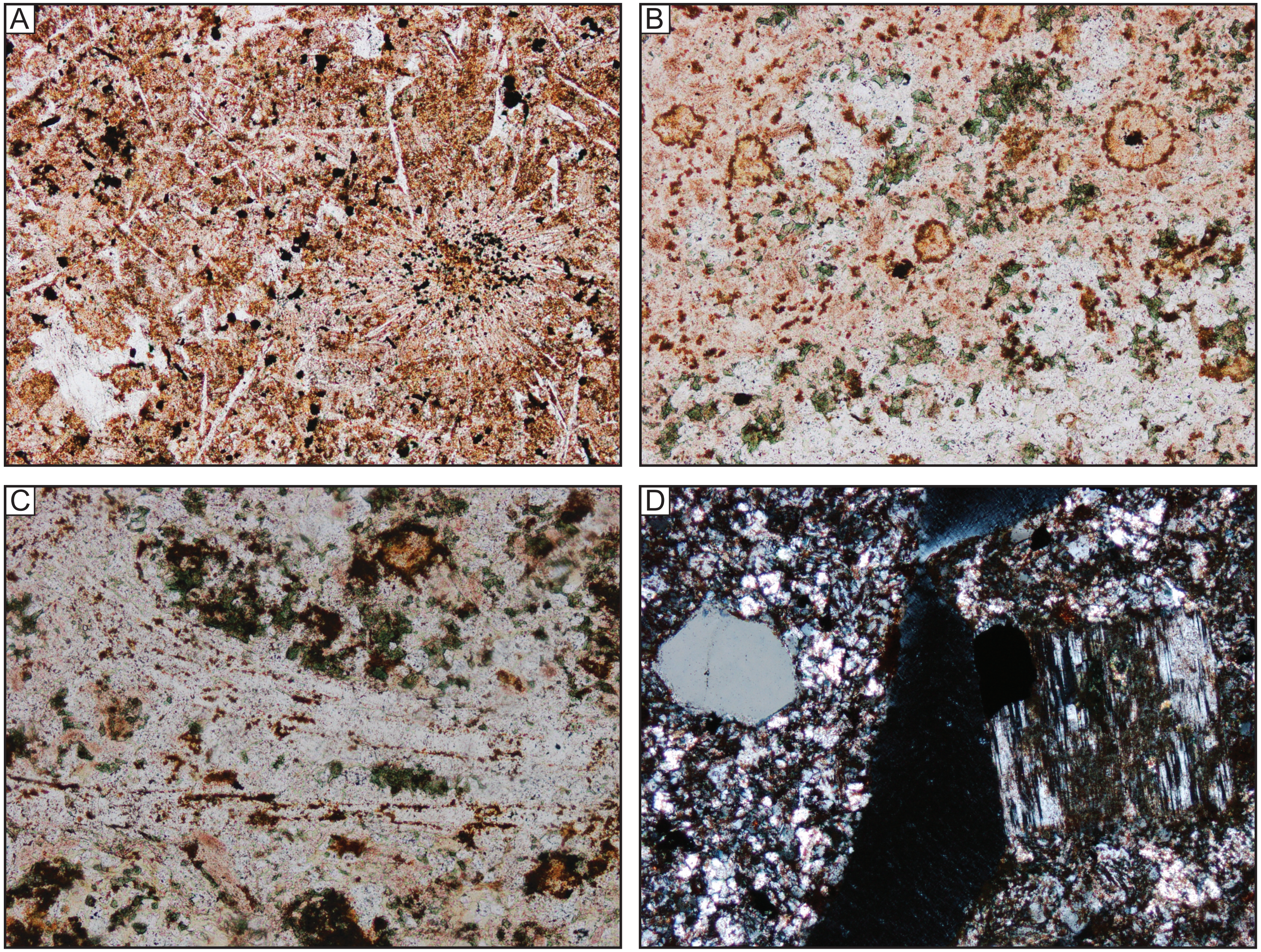

Figure 20. (A) Photomicrograph of rhyolite sample 22-2220 showing well-developed tridymite needles randomly oriented in groundmass or radiating out from spherulites. Plane-polarized light; field of view ~1.3 mm across. (B) Photomicrograph of rhyolite sample 22-1480 showing very fine grained quartzo-feldspathic groundmass and spherulites outlined by very fine grained hematite. Aggregates of green clay are also visible. Plane-polarized light; field of view ~1.3 mm across. (C) Photomicrograph of rhyolite sample 22-1480 showing relict flow lamination defined by laminae of intergrown quartz and feldspar with strands of Fe-Ti oxide granules altering to hematite at their centers. Aggregates of green clay are also visible. Plane-polarized light; field of view ~1.3 mm across. (D) Photomicrograph of rhyolite sample 22-1720 showing chessboard albite (to right) and a subhedral quartz phenocryst (to left). Groundmass consists of intergrown quartz and feldspar. Crossed polars; field of view ~1.3 mm across.

rhyolite field. The samples of the lower flow in the ETH cluster very tightly in the diagram. This provides further evidence that the spread in silica values for this unit is a result of silicification and indicates that the flow represents a chemically homogeneous batch of magma. Samples of the lower flow also cluster tightly with three of the rhyolite lavas from the KFWNC well and the Type III intrusion, indicating that these units are petrogenetically closely linked. The Type IV intrusion plots as a trachyte, which conflicts with its relatively high silica content (76.65 wt %) because trachytes typically have silica contents <69 wt % (Le Bas et al., 1986). There is no petrographic evidence for significant addition of secondary silica in this sample, and in this case the Winchester and Floyd (1977) diagram apparently has not classified the sample appropriately.

Bivariate plots of the incompatible trace elements Nb, Th, Y, and Zr are shown in Figures 25B, 25C, and 25D. As mentioned before, these elements are resistant to secondary alteration, and in many cases they show strong positive correlations in suites of petrogenetically related rocks. Distinct linear trends of this type are lacking in the present case, however, and all of the felsic samples from the KFWNC well and the ETH (except the Type IV intrusion) plot in the same three groups as seen in the Harker diagrams in Figure 24.

All of the felsic samples are shown on normalized multi-element and REE diagrams in Figures 26A and 26B. For the sake of clarity, rhyolite flows from the ETH and the KFWNC well are shown separately in Figures 26C and 26D as are the ETH felsic intrusions in Figures 26E and 26F. All of the samples exhibit Sr, Eu, P, and Ti depletions (Figs. 26A and 26B), consistent with fractionation of plagioclase, apatite, and titanomagnetite. The felsic hypabyssal intrusions in the ETH also show Ba depletions (Fig. 26E), although this is least pronounced in the Type III intrusion. In general, the Type III intrusion and the rhyolite flows in the ETH and the KFWNC well show similar patterns to each other on both the multi-element and REE diagrams, further supporting assignment of these units to a single geochemical group (cf. Figs. 24 and 25B, 25C, and 25D). Note that in Figure 26C the rhyolites in the KFWNC well tend to plot more closely with the lower flow in the ETH than with the upper flow, consistent with other evidence that the lower flow is more closely related petrogenetically to some of the KFWNC rhyolites than it is to the upper flow (cf. Fig. 25A).

Similar conclusions can be reached using the discrimination diagrams in Figures 27A and 27B, where the upper and lower rhyolite flows and the Type III intrusion in the ETH cluster tightly with some of the KFWNC rhyolite lavas, and the Type I and Type II intrusions tend to plot separately from the rest of the data. Note that the Type II intrusions plot off the scale of Figure 27B. Figures 27C, 27D, and 27E suggest that the Type 1, Type II, and Type IV intrusions and two of the KFWNC rhyolites were derived from ocean-island-basalt (OIB)-type sources, whereas older crust was involved in the petrogenesis of the other Arbuckle units.

DIABASE GEOCHEMISTRY

Geochemical analyses of seven diabase intrusions in the ETH are presented in Table 3, and the major oxides are shown in Harker diagrams in Figure 28. The samples have a range in silica content of 47.42 to 51.63 wt %, and most of the major oxides show little correlation with silica. However, K_2O shows a strong increase with silica, whereas CaO shows a corresponding decrease. Samples with the highest K_2O and lowest CaO values show the most intense sericitization of plagioclase in thin section, and we infer that the trends shown by these two oxides partly reflect addition of K_2O and loss of CaO during alteration.

Ignoring the more mobile elements such as Cs, Rb, and K, the trace element contents for all seven diabase intrusions in the ETH compare closely on the multi-element diagram (Fig. 29A), except that one sample (388; Table 3) has higher Th than the other samples. REE patterns for the diabases are also very similar and show LREE enrichment typical of within-plate basalts (Fig. 29B), with slight positive or negative Eu anomalies reflecting minor plagioclase accumulation or fractionation. These trace-element data suggest that the ETH diabases were derived from a single, relatively uniform magma reservoir. In Figure 29A all of the samples show overall negative slopes in the right part of the diagram and, except for sample 388, lack negative Nb-Ta anomalies. These patterns are typical of basalts derived from OIB-type sources (e.g., Pearce, 1982; Sun and McDonough, 1989). The diabases also consistently fall in fields for within-plate, alkaline or transitional basalts on standard discrimination diagrams using immobile trace elements (Fig. 30).

DISCUSSION

Two thick rhyolite lavas make up the major part of the Carlton Rhyolite Group exposed in the ETH and show markedly different features. The upper rhyolite flow is surprisingly thick (>600 m) and, except for a thin basal zone with flow lamination, there is little indication of flow band-

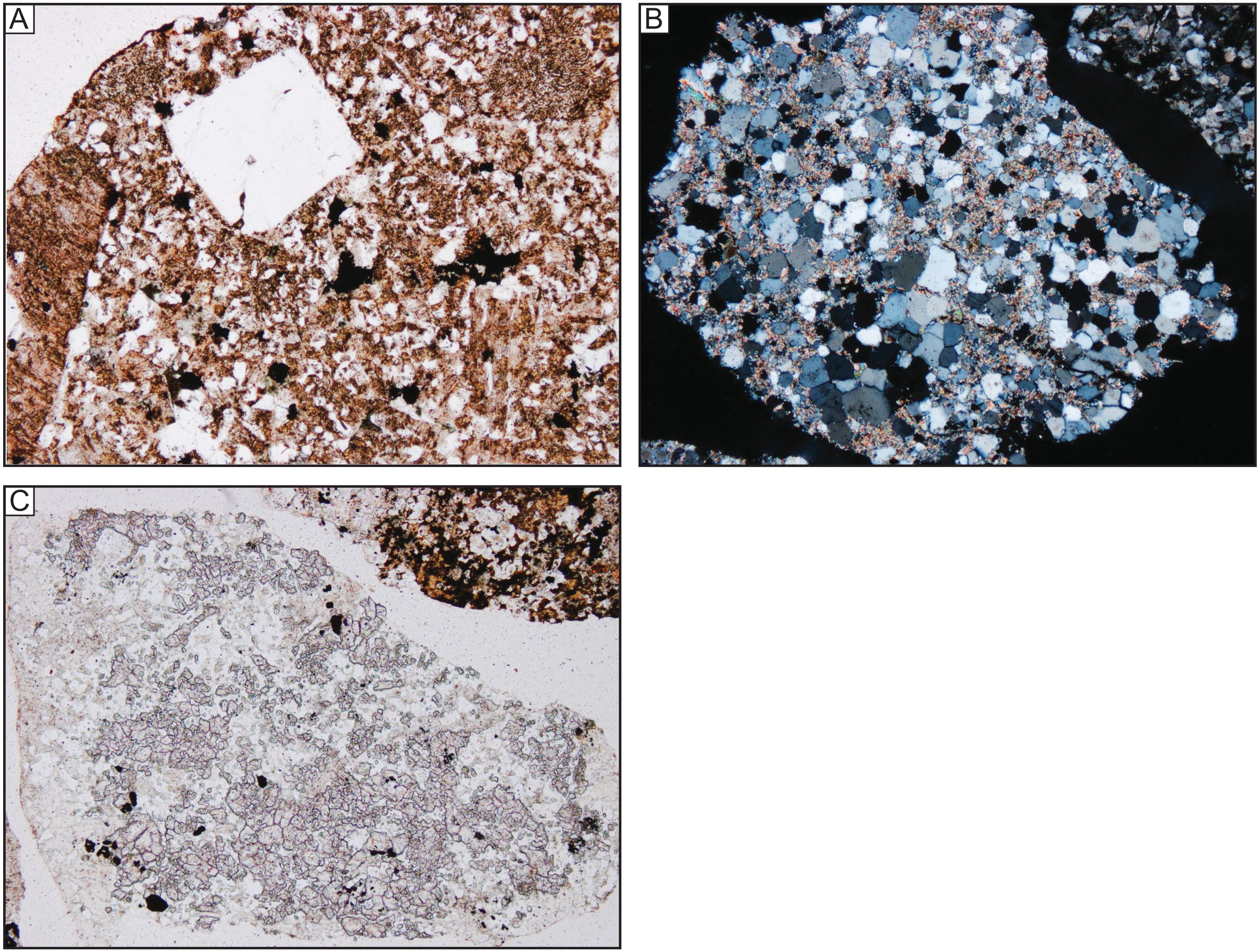

Figure 21. (A) Photomicrograph of hypabyssal felsic intrusion sample 22-2510 showing euhedral quartz phenocryst and chessboard albite to left within a micrograngranophyric groundmass. Plane-polarized light; field of view ~2.5 mm across. (B) Photomicrograph of rhyolite sample 22-4160 showing granoblastic quartz intergrown with alkali feldspar (almost completely altered to sericite). Crossed polars; field of view ~2.5 mm across. (C) Photomicrograph of rhyolite sample 22-4160 showing anhedral to subhedral andalusite intergrown with quartz. Plane-polarized light; field of view ~2.5 mm across.

TABLE 3: GEOCHEMICAL DATA FOR EAST TIMBERED HILLS FELSIC AND DIABASE SAMPLES

Rhyolite flows in the East Timbered Hills

	Upper Flow						**Lower Flow**		
Normalized major elements (wt %)*									
Sample:	**277**	**281**	**298**	**375**	**389**	**392**	**272**	**285**	**290**
SiO_2	73.99	74.56	74.38	75.86	73.85	77.37	74.45	77.58	76.24
TiO_2	0.41	0.39	0.39	0.29	0.38	0.29	0.24	0.21	0.24
Al_2O_3	12.38	12.53	12.49	12.17	12.49	12.35	12.60	10.32	11.92
FeO	3.26	3.35	3.32	2.86	3.55	1.55	3.42	2.92	2.71
MnO	0.11	0.07	0.07	0.03	0.06	0.04	0.03	0.03	0.08
MgO	0.13	0.15	0.30	0.05	0.55	0.14	0.03	0.06	0.00
CaO	1.29	0.37	0.66	0.09	0.46	0.11	0.41	0.06	0.09
Na_2O	4.09	4.18	3.84	3.47	4.30	3.77	3.94	0.08	3.67
K_2O	4.28	4.34	4.49	5.13	4.31	4.34	4.86	8.73	5.04
P_2O_5	0.06	0.06	0.06	0.03	0.05	0.03	0.02	0.01	0.02
LOI**	1.47	0.66	1.10	0.61	0.67	0.77	0.78	0.62	0.43
Total***	97.97	98.71	98.05	98.32	98.46	98.58	98.95	98.53	98.28
Trace elements (ppm)									
Ni	3.31	3.61	2.91	2.70	1.80	2.10	2.41	2.81	0.90
Cr	3.51	2.51	2.91	1.80	2.30	3.10	2.31	3.92	2.31
Sc	5.93	5.53	5.86	3.78	5.30	3.76	3.36	2.99	3.42
V	5.52	4.32	5.02	3.90	5.10	1.90	2.71	3.82	0.70
Ba	956.17	1094.46	1036.90	1013.76	931.80	865.53	804.61	921.82	1206.63
Rb	117.06	113.98	118.89	123.85	108.63	102.62	127.37	224.99	122.57
Sr	72.86	73.56	65.18	46.70	57.39	41.86	35.53	24.73	27.72
Zr	705.49	704.53	696.14	621.93	685.98	633.85	784.07	678.37	781.35
Y	90.87	91.94	110.23	100.92	82.39	104.35	112.88	90.53	110.90
Nb	56.70	57.02	56.57	58.89	56.67	58.87	67.50	57.00	66.03
Ga	22.49	23.39	22.69	22.40	23.50	23.10	27.51	14.86	24.20
Cu	5.72	3.82	2.61	1.70	3.70	3.60	1.41	4.32	2.51
Zn	83.23	108.93	82.33	7.50	107.40	81.20	81.12	51.81	37.15
Pb	13.34	14.41	6.62	7.71	14.11	11.72	7.98	8.96	6.34
La	73.28	78.35	86.66	107.49	47.73	93.48	91.93	74.18	135.11
Ce	164.97	160.72	168.88	173.06	105.98	174.10	168.55	125.84	182.45
Th	10.92	11.17	10.94	11.77	11.09	12.04	12.13	10.41	12.19
Nd	81.85	85.16	91.84	109.13	55.21	102.38	100.34	83.20	132.74
U	3.01	2.97	2.83	3.11	3.03	3.23	3.19	2.69	3.51
Pr	20.36	21.26	22.65	27.26	13.80	25.37	24.68	21.10	33.66
Sm	18.24	19.29	20.53	23.28	12.73	23.13	22.33	17.92	28.12
Eu	3.74	3.93	4.33	3.96	2.70	4.00	3.68	2.88	4.58
Gd	17.10	17.93	20.67	21.64	12.59	22.23	21.28	15.75	25.15
Tb	2.90	3.02	3.34	3.42	2.35	3.59	3.55	2.76	3.90
Dy	18.00	18.29	19.80	20.15	15.80	21.08	21.78	17.50	22.65
Ho	3.58	3.66	3.96	3.97	3.37	4.10	4.38	3.55	4.36
Er	9.86	9.99	10.52	10.68	9.63	10.83	11.87	9.79	11.78
Tm	1.45	1.49	1.50	1.54	1.45	1.56	1.76	1.45	1.72
Yb	8.99	9.19	9.33	9.62	9.07	9.72	10.89	9.02	10.46
Lu	1.37	1.41	1.44	1.44	1.39	1.50	1.64	1.38	1.60
Hf	17.97	17.95	17.64	16.59	17.64	17.08	20.00	17.63	20.17
Ta	3.64	3.71	3.70	3.87	3.67	3.88	4.27	3.74	4.25
Cs	0.87	1.13	0.88	1.37	0.92	0.91	0.78	0.91	0.45

TABLE 3: GEOCHEMICAL DATA FOR EAST TIMBERED HILLS FELSIC AND DIABASE SAMPLES, CONTINUED

Hypabyssal Felsic Intrusions in the East Timbered Hills

	Type I				Type II		Type III	Type IV
Normalized major elements (wt %)*								
Sample:	**279**	**286**	**320b**	**391**	**323**	**324**	**267**	**282e**
SiO_2	79.16	78.06	78.27	78.01	77.31	77.83	75.86	76.65
TiO_2	0.13	0.13	0.13	0.14	0.22	0.23	0.24	0.26
Al_2O_3	10.47	10.96	11.08	11.12	10.89	10.94	11.90	12.38
FeO	2.41	2.66	2.34	2.50	4.44	3.71	3.23	1.33
MnO	0.01	0.01	0.03	0.01	0.01	0.01	0.09	0.02
MgO	0.04	0.11	0.08	0.10	0.20	0.25	0.00	0.08
CaO	0.07	0.15	0.05	0.07	0.08	0.07	0.10	0.10
Na_2O	2.46	2.67	3.32	2.66	1.48	1.69	4.01	2.93
K_2O	5.24	5.25	4.70	5.38	5.34	5.27	4.56	6.24
P_2O_5	0.01	0.00	0.00	0.01	0.01	0.01	0.02	0.02
LOI**	0.63	0.68	0.43	0.74	1.49	1.33	0.30	0.49
Total***	98.68	98.15	98.40	97.43	97.35	97.41	98.98	99.09
Trace elements (ppm)								
Ni	2.81	2.21	1.61	1.30	2.91	2.71	3.01	3.01
Cr	4.22	3.21	3.82	2.80	3.71	4.32	3.82	2.91
Sc	0.07	0.08	0.22	0.02	0.41	0.38	3.39	2.21
V	4.72	3.11	2.01	4.40	0.10	2.91	2.21	1.31
Ba	67.32	57.13	71.92	71.00	171.87	134.72	917.69	496.39
Rb	153.24	158.42	136.25	177.48	159.53	143.67	114.89	196.08
Zr	779.48	810.37	790.22	831.36	2022.00	2016.91	776.07	322.57
Y	121.99	106.95	101.70	111.42	189.60	211.17	109.46	61.49
Nb	150.23	161.11	151.75	182.78	278.01	264.66	66.76	96.81
Ga	21.69	22.29	25.20	28.90	31.53	31.32	25.20	16.97
Cu	15.46	4.22	9.54	5.40	5.12	3.92	5.12	2.71
Zn	15.76	27.61	31.53	39.70	147.09	76.00	24.30	41.47
Pb	11.95	5.98	4.82	15.37	22.51	18.31	15.04	43.11
La	116.70	82.11	84.31	115.84	94.80	171.97	103.45	81.35
Ce	126.81	172.22	177.93	149.12	235.68	247.60	193.42	184.85
Th	20.60	20.50	20.87	23.21	28.83	28.93	12.11	20.34
Nd	110.27	81.40	83.53	112.40	108.98	177.55	110.07	65.53
U	4.58	4.30	4.67	4.95	7.34	7.67	3.45	4.66
Pr	29.79	21.67	22.35	30.24	27.97	45.68	27.28	19.04
Sm	24.86	19.16	19.23	24.98	26.27	39.97	24.12	12.48
Eu	0.33	0.22	0.24	0.35	1.27	1.79	3.95	1.03
Gd	21.56	17.73	17.34	21.82	24.93	36.71	22.65	9.96
Tb	3.49	3.05	3.05	3.55	5.02	6.57	3.66	1.85
Dy	20.77	19.02	19.19	21.83	35.26	40.92	21.93	12.06
Ho	4.21	3.97	3.98	4.48	7.69	8.36	4.30	2.46
Er	11.90	11.23	11.35	12.66	22.64	23.35	11.60	7.12
Tm	1.79	1.72	1.72	1.90	3.41	3.43	1.71	1.10
Yb	11.21	10.73	10.83	12.01	21.31	21.41	10.59	7.00
Lu	1.68	1.63	1.61	1.82	3.23	3.23	1.61	1.05
Hf	22.81	23.50	22.74	25.20	45.99	46.09	20.21	9.92
Ta	10.47	10.95	10.48	11.98	17.45	17.43	4.29	6.80
Cs	0.45	0.40	0.34	0.61	0.76	0.62	0.26	0.45

TABLE 3: GEOCHEMICAL DATA FOR EAST TIMBERED HILLS FELSIC AND DIABASE SAMPLES, CONTINUED

Diabase Intrusions in the East Timbered Hills

Normalized major elements (wt %)*

Sample:	**274**	**282A**	**318**	**369**	**386**	**387**	**388**
SiO_2	50.08	49.16	49.26	50.08	47.47	47.42	51.63
TiO_2	1.92	2.14	2.47	1.63	2.11	2.07	2.12
Al_2O_3	13.99	14.36	13.66	16.02	15.63	15.68	14.35
FeO	13.61	12.73	13.69	11.95	12.93	12.66	12.12
MnO	0.21	0.23	0.23	0.20	0.23	0.23	0.23
MgO	6.26	6.77	6.59	5.72	7.51	7.57	6.67
CaO	9.19	10.21	9.38	9.24	10.59	10.74	7.41
Na_2O	2.51	2.56	2.73	2.67	2.38	2.30	2.67
K_2O	1.88	1.39	1.48	2.18	0.88	1.08	2.47
P_2O_5	0.36	0.45	0.51	0.32	0.27	0.26	0.34
LOI**	1.31	1.83	1.28	2.00	1.57	1.82	2.21
Total***	98.92	98.26	98.58	97.58	98.64	97.27	96.92
Trace elements (ppm)							
Ni	51.94	61.91	58.72	56.30	88.70	85.40	58.5
Cr	46.36	118.44	91.72	44.10	78.80	87.90	82.3
Sc	40.71	40.54	41.02	32.66	33.03	36.25	36.79
V	338.28	307.87	342.77	290.10	307.90	310.20	303.6
Ba	366.18	449.38	515.45	424.15	335.17	362.67	723.50
Rb	105.08	63.87	55.80	80.42	35.67	50.30	116.59
Sr	428.06	468.74	451.38	392.20	449.66	478.01	466.53
Zr	110.06	115.63	136.12	100.56	103.17	95.51	149.95
Y	24.30	24.36	27.83	22.01	19.90	19.20	27.74
Nb	19.76	19.11	22.16	17.89	18.90	17.50	24.50
Ga	17.75	17.65	18.84	18.70	19.00	19.40	18.10
Cu	162.41	120.34	125.82	135.00	150.70	164.10	110.80
Zn	109.47	106.88	147.76	110.10	105.50	112.10	117.00
Pb	4.14	3.45	5.35	9.11	6.51	17.71	5.79
La	21.05	20.63	23.68	18.70	16.72	15.66	31.29
Ce	43.65	44.54	50.94	39.35	36.61	34.41	64.26
Th	1.85	1.18	1.58	1.74	1.30	1.17	4.01
Nd	23.20	25.14	28.26	20.82	20.75	19.70	31.19
U	0.45	0.30	0.39	0.42	0.35	0.31	0.90
Pr	5.57	5.92	6.76	4.99	4.83	4.58	7.86
Sm	5.21	5.52	6.19	4.61	4.65	4.43	6.32
Eu	1.77	2.00	2.26	1.57	1.71	1.66	1.78
Gd	4.94	5.23	5.90	4.50	4.61	4.34	5.79
Tb	0.80	0.82	0.93	0.72	0.71	0.69	0.92
Dy	4.76	4.87	5.52	4.38	4.27	4.05	5.53
Ho	0.98	0.99	1.12	0.89	0.81	0.79	1.08
Er	2.58	2.64	2.98	2.36	2.12	2.04	2.97
Tm	0.37	0.36	0.43	0.33	0.29	0.28	0.42
Yb	2.27	2.27	2.56	2.07	1.75	1.70	2.62
Lu	0.35	0.35	0.40	0.33	0.26	0.27	0.42
Hf	2.79	2.81	3.32	2.55	2.69	2.48	3.82
Ta	1.24	1.17	1.38	1.10	1.24	1.14	1.54
Cs	3.38	0.36	0.61	0.77	0.68	0.62	0.89

TABLE 3: GEOCHEMICAL DATA FOR EAST TIMBERED HILLS FELSIC AND DIABASE SAMPLES, CONTINUED

Rhyolites in the Kaiser Francis-Westheimer Neustadt 1 Chapman well

Normalized major elements (wt %)*

Sample:	**22-1**	**22-2**	**22-3**	**22-4**	**22-5**
SiO_2	76.39	76.39	75.67	74.85	76.49
TiO_2	0.19	0.19	0.23	0.22	0.21
Al_2O_3	11.99	11.77	11.94	12.63	12.19
FeO	2.43	2.85	3.17	2.50	1.96
MnO	0.03	0.02	0.03	0.04	0.02
MgO	0.21	0.09	0.11	0.11	0.07
CaO	0.56	0.26	0.24	0.99	0.41
Na_2O	3.54	3.55	3.72	4.03	3.40
K_2O	4.64	4.85	4.86	4.62	5.23
P_2O_5	0.01	0.02	0.02	0.02	0.02
LOI**	1.42	0.82	0.22	1.31	0.92
Total***	97.36	98.36	99.51	97.95	97.92

Trace elements (ppm)

Ni	3.90	2.90	1.60	4.00	3.40
Cr	9.10	2.60	3.20	10.40	8.60
Sc	2.82	2.79	3.62	1.60	1.25
V	9.00	5.70	2.20	5.20	3.50
Ba	926.25	935.19	1116.39	1367.03	1347.17
Rb	117.00	123.91	117.62	116.05	123.56
Sr	43.51	36.54	39.43	53.19	39.48
Zr	710.85	712.05	779.62	687.44	666.79
Y	92.06	94.32	104.33	96.56	96.97
Nb	54.26	52.48	59.27	89.69	87.21
Ga	21.10	19.70	22.60	22.90	22.70
Cu	7.80	7.70	6.10	9.70	6.20
Zn	132.80	30.50	34.80	67.10	89.30
Pb	10.45	12.10	14.05	13.19	13.80
La	71.51	77.55	79.86	96.56	94.91
Ce	158.79	172.97	177.82	206.81	202.74
Th	11.57	11.62	11.75	10.78	10.59
Nd	79.29	87.02	90.00	98.17	96.66
U	2.73	2.85	3.31	2.73	2.46
Pr	20.07	21.83	22.58	25.35	24.83
Sm	18.05	19.45	20.26	20.40	20.43
Eu	2.89	3.26	3.59	3.47	3.42
Gd	16.92	18.30	18.97	18.10	17.96
Tb	2.93	3.05	3.24	3.05	3.06
Dy	18.40	18.71	20.25	18.77	18.73
Ho	3.69	3.70	4.06	3.82	3.80
Er	10.14	10.31	11.26	10.69	10.70
Tm	1.49	1.51	1.66	1.60	1.59
Yb	9.30	9.38	10.17	9.97	9.97
Lu	1.41	1.42	1.54	1.55	1.54
Hf	18.46	18.32	19.80	18.04	17.52
Ta	3.70	3.39	3.81	5.54	5.39
Cs	0.62	0.56	0.51	0.52	0.42

* Major elements are normalized to 100% on a volatile-free basis

** Loss on ignition   ***Total before normalization

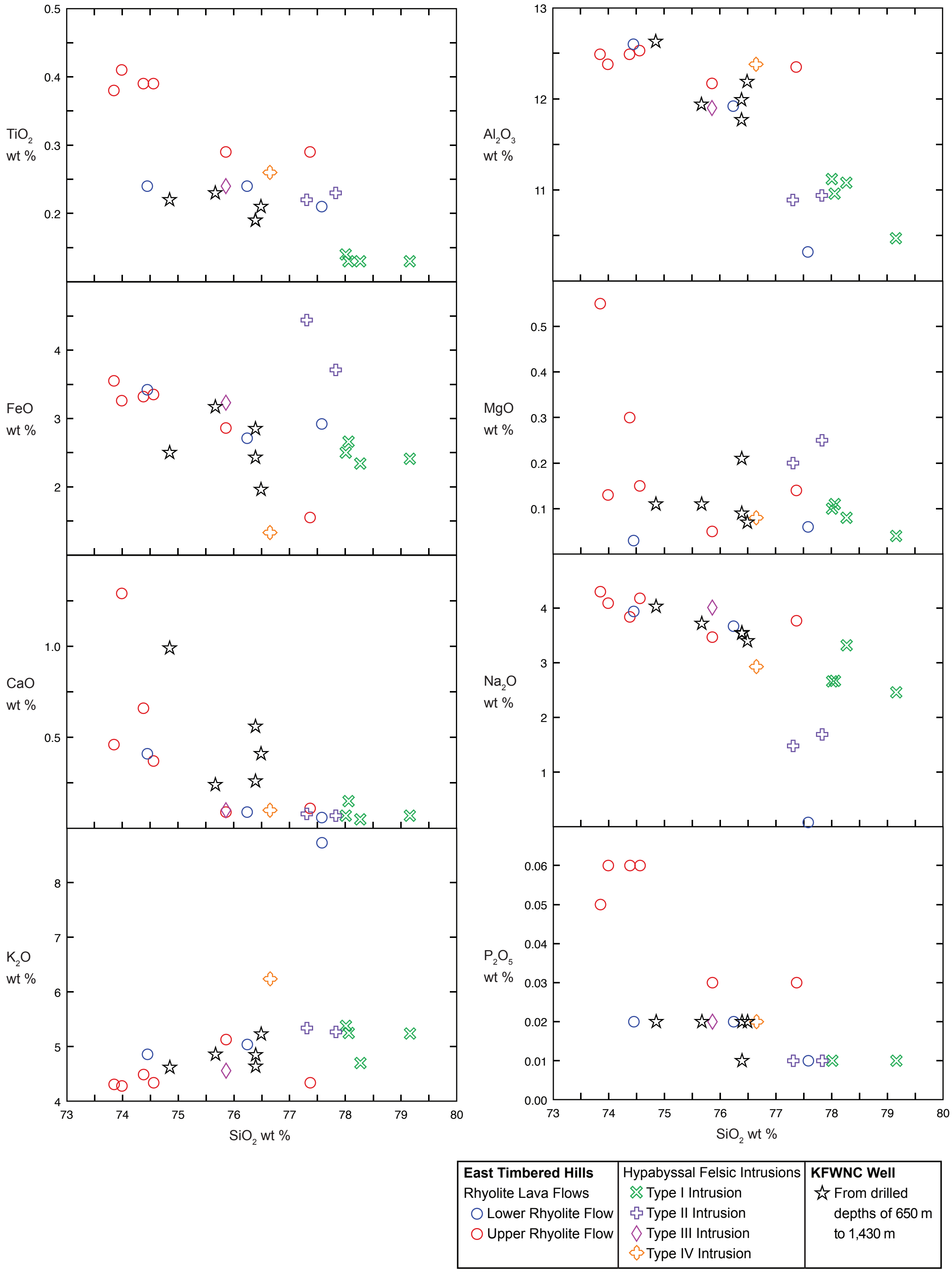

Figure 22. Harker diagrams for major oxides for felsic rocks in ETH and KFWNC well.

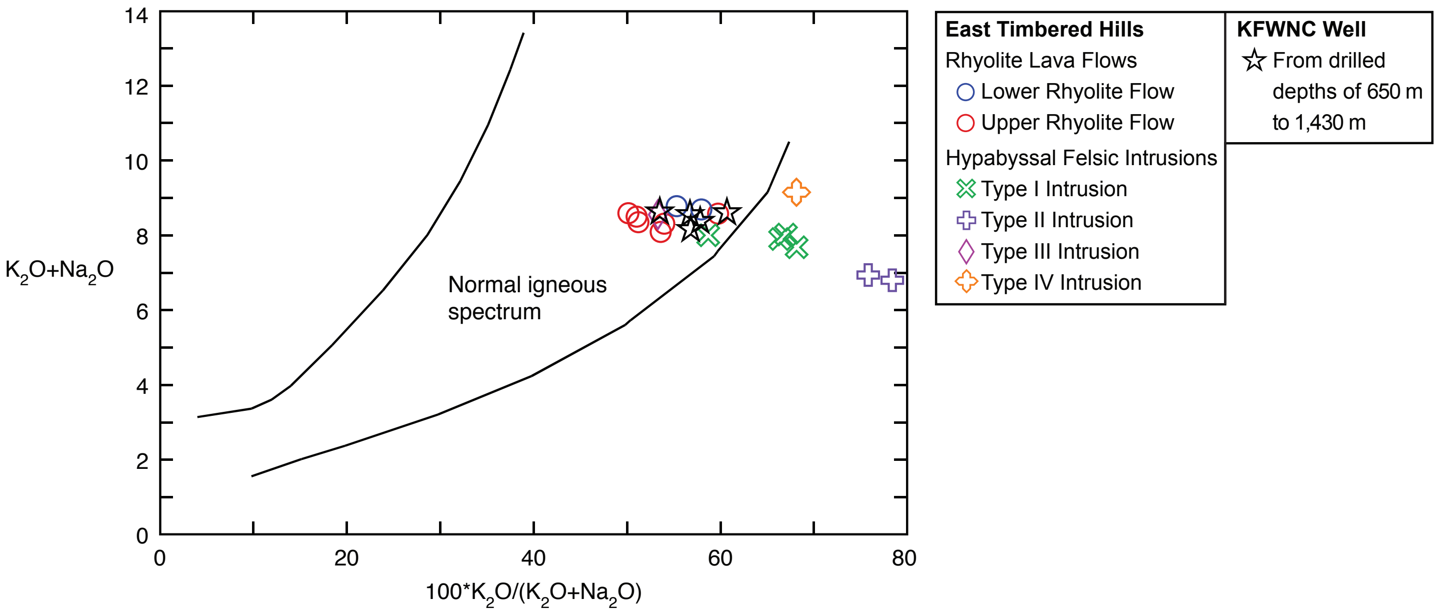

Figure 23. Igneous spectrum diagram of Hughes (1972) for felsic rocks.

ing within the main part of the flow; flow breccia is also lacking. The flow underwent a simple cooling history after emplacement based on the uniformly developed columnar jointing throughout the flow and the progressive increase in size of randomly oriented tridymite needles in the groundmass toward the flow interior, where cooling occurred at the slowest rate.

Geochemical data indicate that the flow records eruption of compositionally heterogeneous magma. However, the simple cooling history after emplacement led to a consistent vertical sequence of textural zones in the flow, with originally glassy zones along the base and top of the flow, which pass inward into spherulitic zones and then into a homogeneous felsitic interior, where the coarsest tridymite needles appear. This vertical textural zonation is similar to that shown by most rhyolite flows in the Wichita Mountains, which are inferred to be remnants of laterally extensive lavas (Hanson and Eschberger, this guidebook). The longest known lava flow in the Wichitas (the Fort Sill rhyolite) can be traced laterally for ~18.5 km, but its total extent may have been considerably greater because the flow is either truncated by intrusive granite or goes beneath Permian and Quaternary cover (Finegan and Hanson, this guidebook). The upper flow in the ETH may have had a similar large extent, although this is now impossible to determine because the flow is truncated by faults along three sides. In any case, it is the thickest rhyolite flow so far documented in the Southern Oklahoma Aulacogen and is substantially thicker than the thickest flow present in the Wichitas (400 m). A likely interpretation is that the flow was ponded against the northern fault-bounded margin of the rift zone, which would have been a short distance north of the present position of the ETH (Ham et al., 1964).

The original dimensions of the lower rhyolite flow in the ETH are also unknown, but with a thickness >300 m it is thicker than all but one of the rhyolite flows documented in the Wichitas. It differs from the upper rhyolite flow and from most flows in the Wichitas in that it is pervasively flow banded and has thick flow breccia at the top. Much of the flow remained glassy after early high-temperature devitrification, even in the flow interior, and tridymite needles are lacking. These characteristics suggest that the unit represents a laterally restricted lava dome or coulee that underwent relatively rapid cooling. Unlike the upper flow, the lower flow represents extrusion of chemically homogeneous magma.

A significant pause in eruptive activity in the area is recorded by the 60-m-thick bedded volcaniclastic sequence that separates the two flows. Planar-laminated tuff within the sequence was likely derived from vents located some distance from the study area. Deposition is inferred to have occurred in a lake; otherwise, it is difficult to see how the fine-grained ash beds could have been preserved without being reworked by running water or wind. Intense soft-sediment folding of parts of the sequence may record seismic activity within the developing rift, particularly given the proximity to the northern rift margin. The poorly sorted,

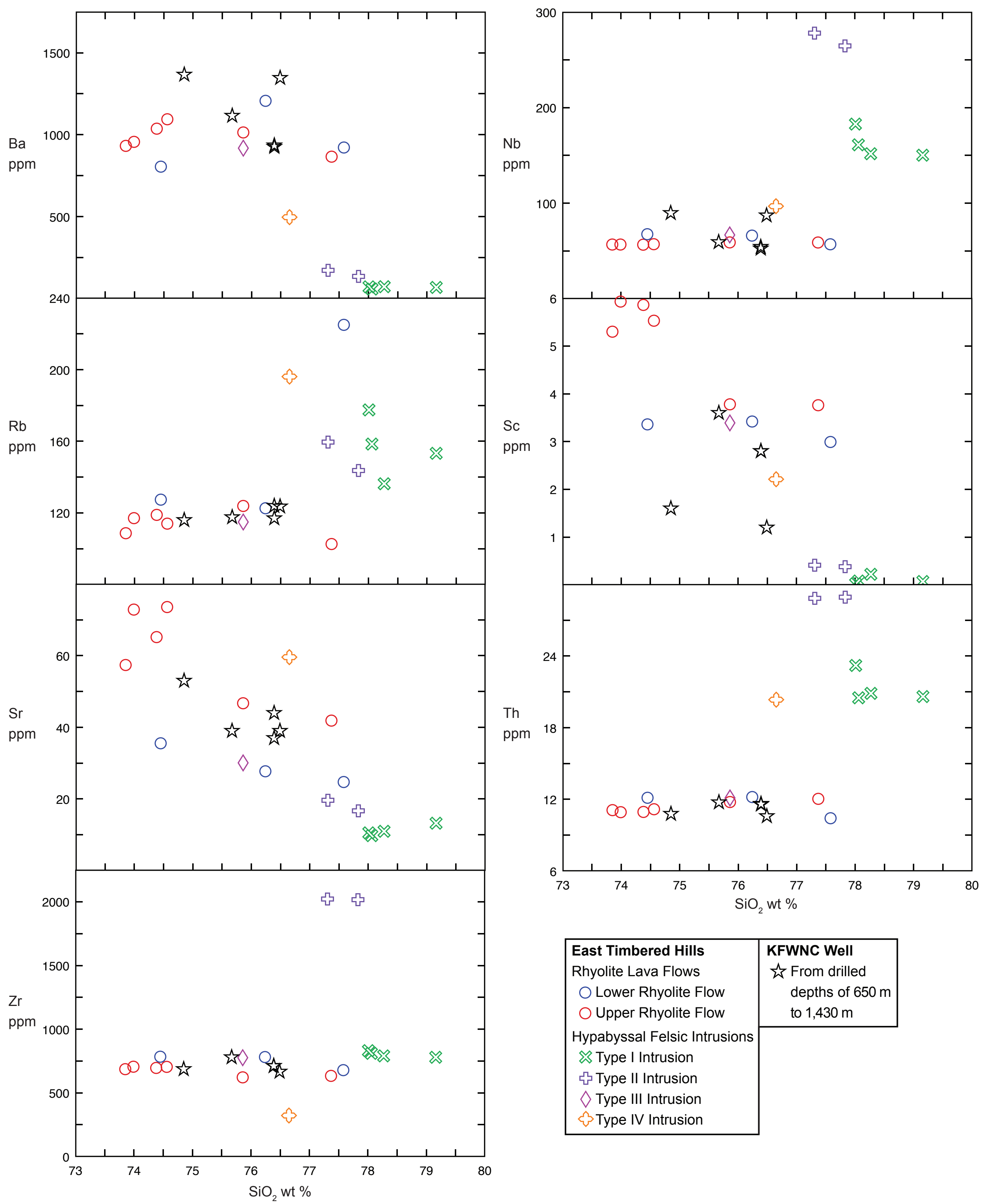

Figure 24. Harker diagrams for selected trace elements in felsic rocks.

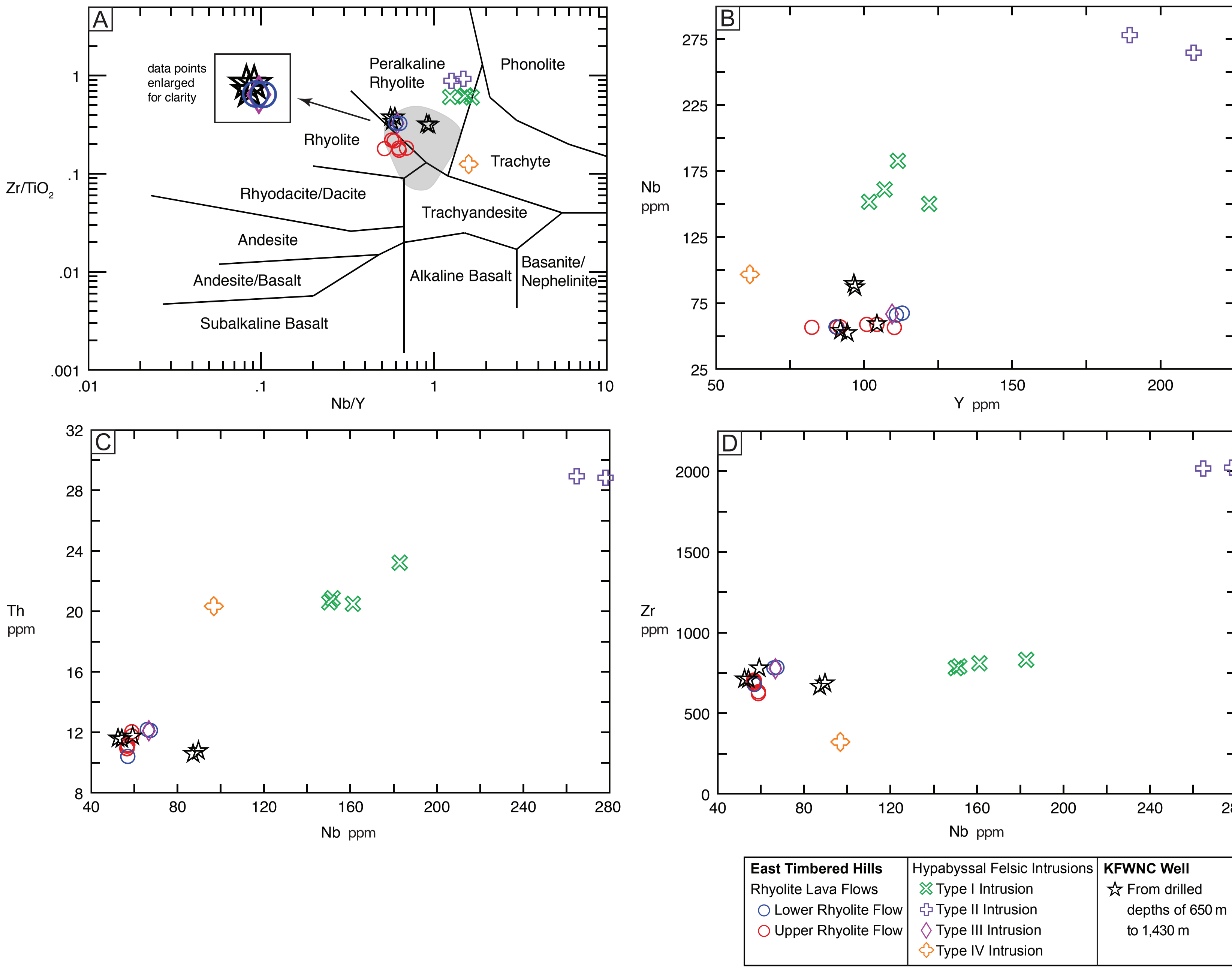

Figure 25. (A) Data for felsic rocks plotted on discrimination diagram of Winchester and Floyd (1977). Data for Carlton Rhyolite in the Wichita Mountains are shown by gray field and are from Finegan and Hanson (this guidebook) and Hanson et al. (this guidebook). (B) Plot of Nb versus Y for felsic rocks. (C) Plot of Th versus Nb for felsic rocks. (D) Plot of Zr versus Nb for felsic rocks.

massively bedded conglomerate units in the upper part of the sequence are inferred to represent debris-flow deposits emplaced within the lake. The presence of a thin peperite zone at the base of the upper flow indicates that the lacustrine deposits were still wet and unconsolidated when the lava moved across them. However, the flow shows no evidence for large-scale interaction with external water, suggesting that the lake may have contained little water when the lava encountered it.

In the KFWNC well to the southeast of the ETH, fourteen rhyolite flows occur over a depth of ~1.15 km. These flows show some petrographic similarities to the two flows in the ETH, but it is not possible to find a complete match in groundmass texture and phenocryst content between the two exposed flows and any of the subsurface examples. Overall, the volcanic stratigraphy exposed in the ETH cannot be traced into the KFWNC well. This may reflect lateral facies changes in the rhyolitic volcanic succession over that distance or offset between the two areas along Pennsylvanian or Cambrian (rift-related) faults.

Hypabyssal felsic intrusions make up an important part of the Carlton Rhyolite exposed in the ETH, and similar intrusions also occur in the KFWNC well. They were clearly emplaced in a shallow, subvolcanic setting, but some cooled slowly enough to develop phaneritic textures. In the ETH, four different lithological and geochemical types of intrusions are present, adding considerably to the compositional diversity of the ETH rhyolites. Similar felsic intrusions locally occur within the Carlton Rhyolite exposed in the Wichita Mountains, but they are rare (Finegan and Hanson, this guidebook; Hanson et al., this guidebook). Their relative abundance in the ETH and adjacent parts of the subsurface suggests that this area was located in a more proximal setting relative to the source vents during development of the rhyolitic volcanic field.

The map patterns of the intrusions exposed in the ETH range from ellipsoidal to highly irregular, and some of these intrusions probably have complicated shapes in three dimensions. It is likely that the smaller intrusions represent offshoots from larger bodies. Why the intrusions developed these complex shapes is unclear. They may have been emplaced during a period of time when tensional stresses in the rift zone were at a minimum so that dike injection was not favored.

Our geochemical data for the rhyolites in the ETH and KFWNC well are compared to available data for the Carlton Rhyolite exposed in the Wichita Mountains in Figures 25A, 26, and 27. In the Winchester and Floyd (1977) diagram (Fig. 25A), some of the Arbuckle samples overlap with the field for the Wichita rhyolites, but a number of the samples fall outside that field, pointing to compositional variations in the felsic magmas emplaced in different parts of the rift zone. The Type I and Type II intrusions fall much farther into the peralkaline field than the other Arbuckle samples, consistent with the highly fractionated nature of these two types of intrusions.

The Arbuckle data show a tendency to cluster into discrete groups in Figure 25A, but these groups are better resolved in bivariate plots of immobile trace elements (Figs. 25B, 25C, and 25D). The rhyolite lavas in the ETH and KFWNC well and the Type III intrusion in the ETH define a single geochemical group in those figures, and we infer that these units were derived from a single source or magma reservoir. Intrusions of Types I, II, and IV represent compositionally distinct magmas.

Normalized multi-element and REE patterns for the Arbuckle felsic rocks generally compare closely with the data for the Carlton Rhyolite in the Wichita Mountains (Fig. 26). However, the Type II intrusions in the ETH typically show higher contents of incompatible trace elements resistant to secondary alteration and much stronger depletions in Ba than seen in any of the rhyolites in the Wichitas (Fig. 26E). The Type I intrusions in the ETH show even more substantial Ba depletion as well as the most pronounced negative Eu anomalies. These two types of intrusions are, in fact, the most highly fractionated rhyolites so far documented in the Wichita igneous province. They also plot farther into the OIB field in Figure 27E, although this could reflect the effects of pyroxene fractionation on the Ce/Nb ratio rather than being a direct indication of source composition (Eby, 1990). It is also interesting to note in this diagram that most of the other Arbuckle data plot significantly closer to average continental crust than the Wichita rhyolites, suggesting that older crust played a more important role in the petrogenesis of the felsic magmas in the Arbuckle region.

Eleven diabase bodies, the majority of which are dikes, have been mapped intruding the rhyolite in the ETH. Additional examples undoubtedly occur in poorly exposed parts of the study area, but the diabases are clearly much less abundant in the ETH than in exposed Mesoproterozoic crystalline rocks near the northern margin of the rift in the eastern Arbuckles, where they occupy as much as ~30% of the rock volume (Hanson et al., 2013, Lidiak et al., paper, this guidebook). Our observations are consistent with those of Denison (1995), who pointed out that the marked difference in the number of diabase intrusions in the Mesoproterozoic basement relative to those intruding Carlton Rhyolite in adjacent areas indicates that most of

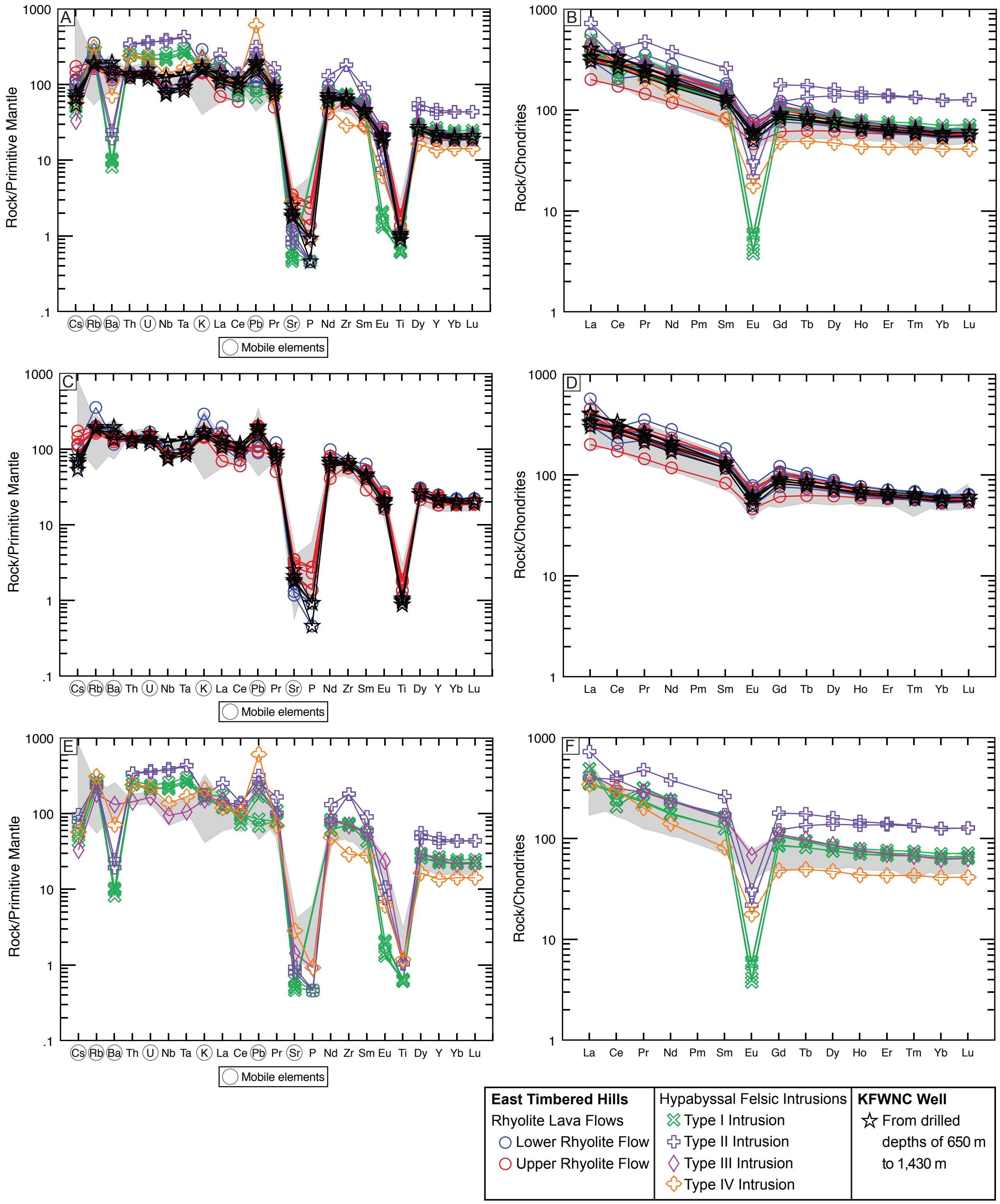

Figure 26. (A) Multi-element diagram for all felsic samples. (B) REE diagram for all felsic samples. (C) Multi-element diagram for rhyolite lava flows in ETH and KFWNC well. (D) REE diagram for rhyolite lava flows in ETH and KFWNC well. (E) Multi-element diagram for hypabyssal felsic intrusions in ETH (Types I–IV). (F) REE diagram for hypabyssal felsic intrusions in ETH (Types I–IV). Normalization values in diagrams are from Sun and McDonough (1989). Data for Carlton Rhyolite in the Wichita Mountains are shown by gray fields; see Figure 25A caption for sources.

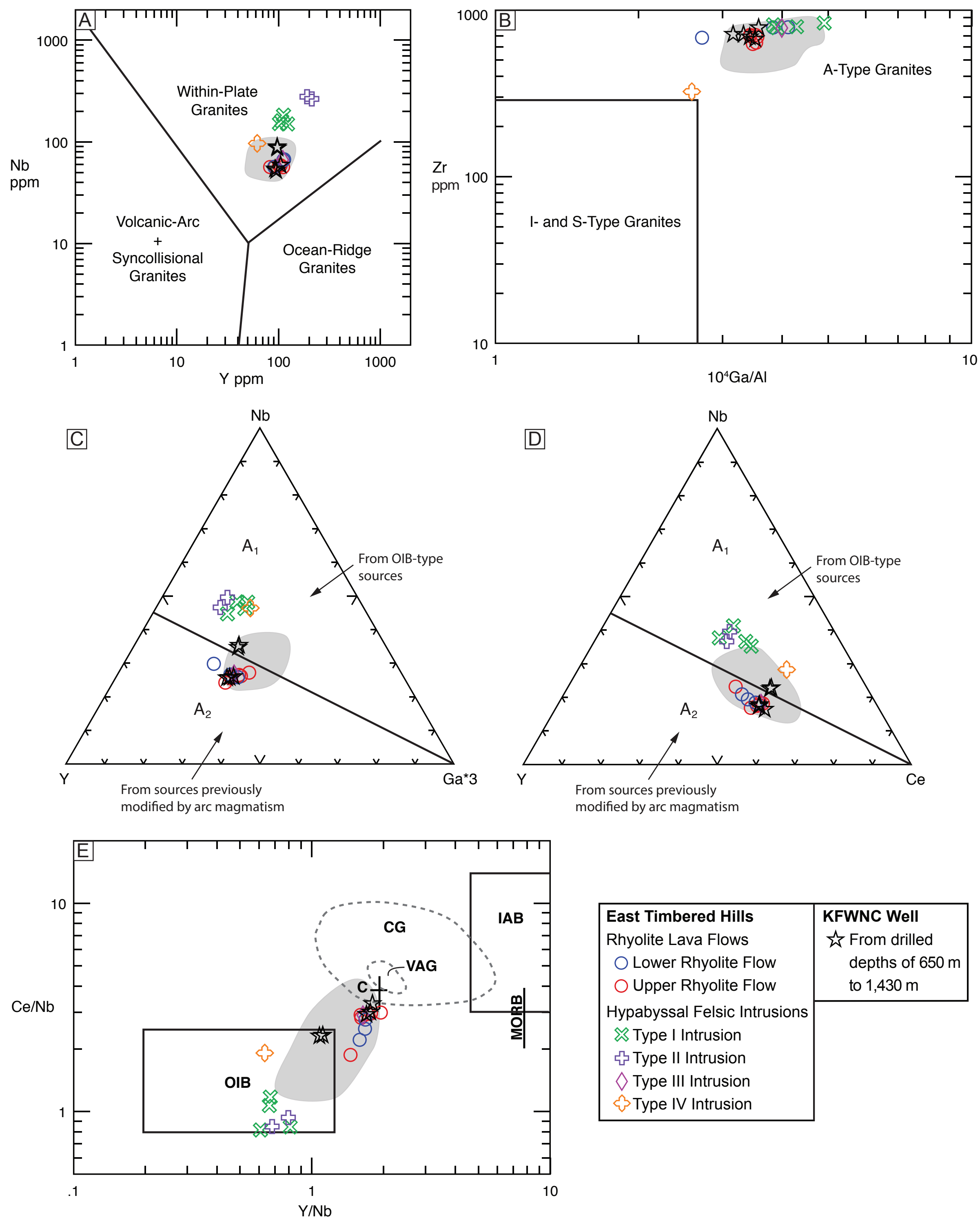

Figure 27. (A) Nb versus Y discrimination diagram of Pearce et al. (1984). (B) Zr versus 10^4Ga/Al discrimination diagram of Whalen et al. (1987). (C) Y-Nb-Ga discrimination diagram of Eby (1992) for A-type felsic rocks. (D) Y-Nb-Ce discrimination diagram of Eby (1992) for A-type felsic rocks. (E) Ce/Nb versus Y/Nb diagram of Eby (1990) for A-type felsic rocks. *MORB*: range for mid-ocean ridge basalts; *IAB*: field for island-arc basalts; cross labeled *C*: average crustal ratios; *CG*: field for syncollisional granite; *VAG*: field for volcanic-arc granite; *OIB*: field for ocean-island basalts. Data for Carlton Rhyolite in the Wichita Mountains are shown by gray fields; see Figure 25A caption for sources.

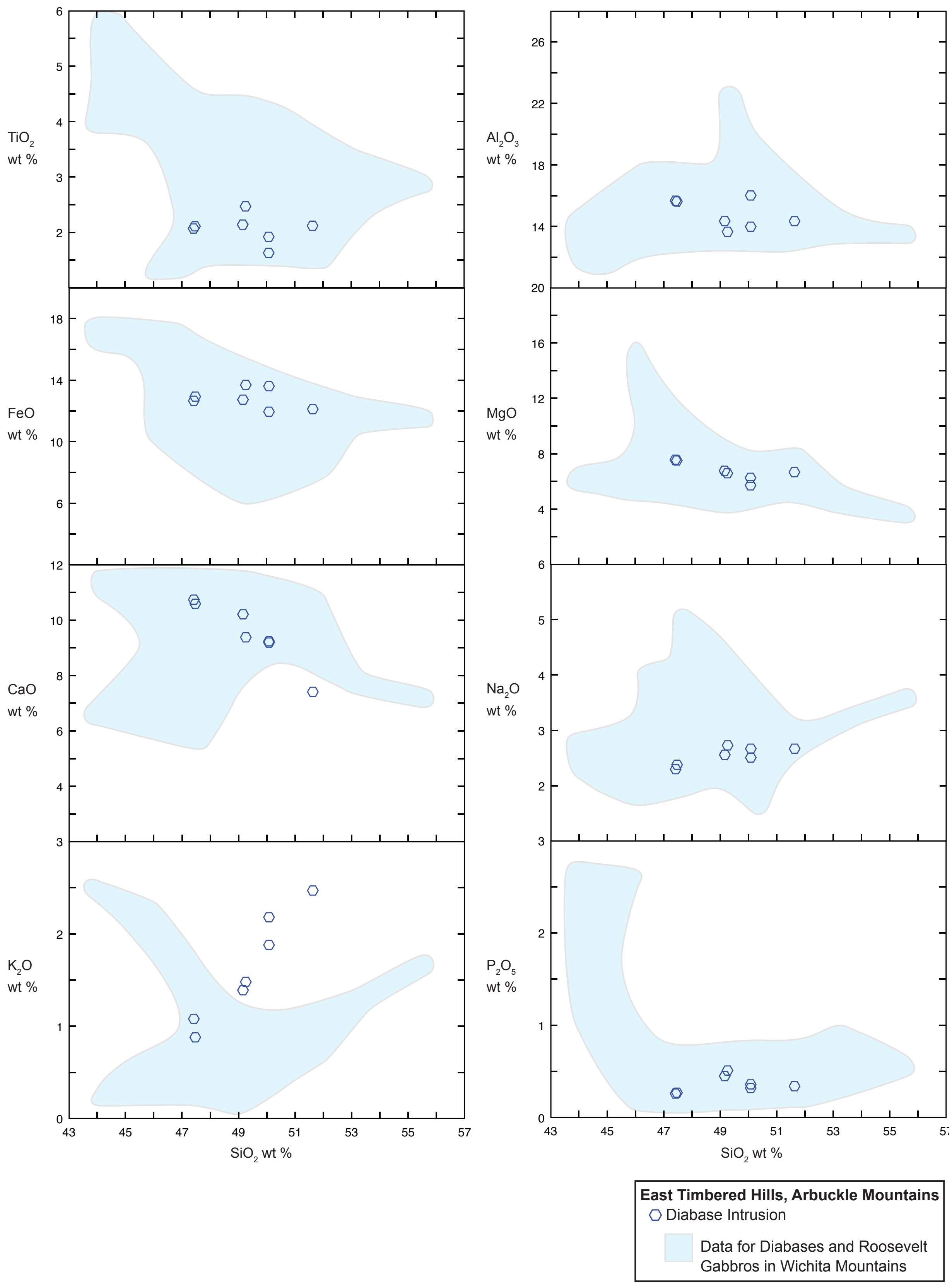

Figure 28. Harker diagrams for major oxides for diabases in ETH. Data for diabase intrusions and Roosevelt gabbros in the Wichita Mountains are from Aquilar (1988), Diez de Medina (1988), and DeGroat et al. (1995).

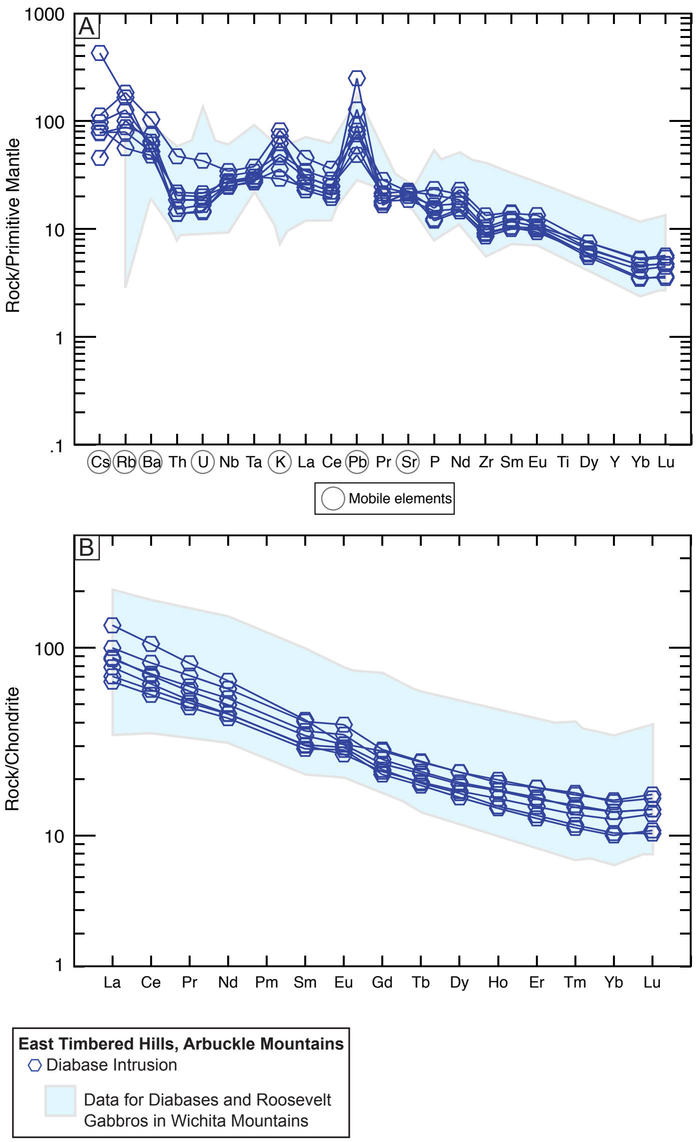

Figure 29. (A) Multi-element diagram for diabase intrusions in ETH. (B) REE diagram for diabase intrusions in ETH. Normalization values in diagrams are from Sun and McDonough (1989). Data for diabase intrusions and Roosevelt gabbros in the Wichita Mountains are from Aquilar (1988) (other data sets from the Wichita Mountains are incomplete).

the dikes were emplaced prior to rhyolite extrusion.

In the ETH, the diabases intrude both the upper and lower rhyolite flows and the intervening bedded volcaniclastic rocks. None have been found close to the hypabyssal felsic intrusions in the area, and temporal relations between the two suites of intrusions are unclear. Both the major- and trace-element contents of the diabases overlap with or plot close to data for diabase intrusions and the Roosevelt gabbros in the Wichita Mountains, although the ETH diabases have lower TiO_2 contents than most of the Wichita samples. In general, our data suggest that the diabases in the ETH and the diabases and Roosevelt gabbros in the Wichitas were derived from similar sources and experienced similar petrogenetic histories in these different parts of the rift.

REFERENCES CITED

Aquilar, J., 1988, Geochemistry of mafic rock units of the Southern Oklahoma Aulacogen, southwestern Oklahoma [M.S. thesis]: Norman, Oklahoma, University of Oklahoma, 167 p.

Bacon, C.R., and Druitt, T.H., 1988, Compositional evolution of the zoned calc-alkaline magma chamber of Mount Mazama, Crater Lake, Oregon: Contributions to Mineralogy and Petrology, v. 98, p. 224-256.

Bull, K.F., and McPhie, J., 2007, Fiamme textures in volcanic successions: Flaming issues of definition and interpretation: Journal of Volcanology and Geothermal Research, v. 164, p. 205-216.

DeGroat, P.J., Donovan, R.N., Hanson, R.E., and Weaver, B.L., 1995, Cambrian diabase and gabbro in the Blue Creek Canyon area, Wichita Mountains, southwestern Oklahoma: Oklahoma Geology Notes, v. 55, p. 168-186.

Denison, R.E., 1995, Significance of air-photograph linears in the basement rocks of the Arbuckle Mountains, *in* Johnson, K.S., ed., Structural Styles in the Southern Midcontinent, 1992 Symposium: Oklahoma Geological Survey Circular 97, p. 119-131.

Diez de Medina, D.M., 1988, Geochemistry of the Sandy Creek Gabbro, Wichita Mountains, Oklahoma [M.S. thesis]: Norman, Oklahoma, University of Oklahoma, 163 p.

Eby, G.N., 1990, The A-type granitoids: A review of their occurrence and chemical characteristics and speculations on their petrogenesis: Lithos, v. 26, p. 115-134.

Eby, G.N., 1992, Chemical subdivision of the A-type granitoids: Petrogenetic and tectonic implications: Geology, v. 20, p. 641-644.

Eschberger, A.M., 2012, Volcanological and geochemical studies of Cambrian rift-related igneous rocks in the western Arbuckle Mountains, southern Oklahoma [M.S. thesis]: Fort Worth, Texas, Texas Christian University, 191 p.

Floyd, P.A., and Winchester, J.A., 1975, Magma type and tectonic setting discrimination using immobile elements: Earth and Planetary Science Letters, v. 27, p. 211-218.

Ham, W.E., 1973, Regional Geology of the Arbuckle Mountains, Oklahoma: Oklahoma Geological Survey Special Publication 73-3, 61 p.

Ham, W.E., Denison, R.E., and Merritt, C.A., 1964, Basement Rocks and Structural Evolution of Southern Oklahoma: Oklahoma Geological Survey Bulletin 95, 302 p.

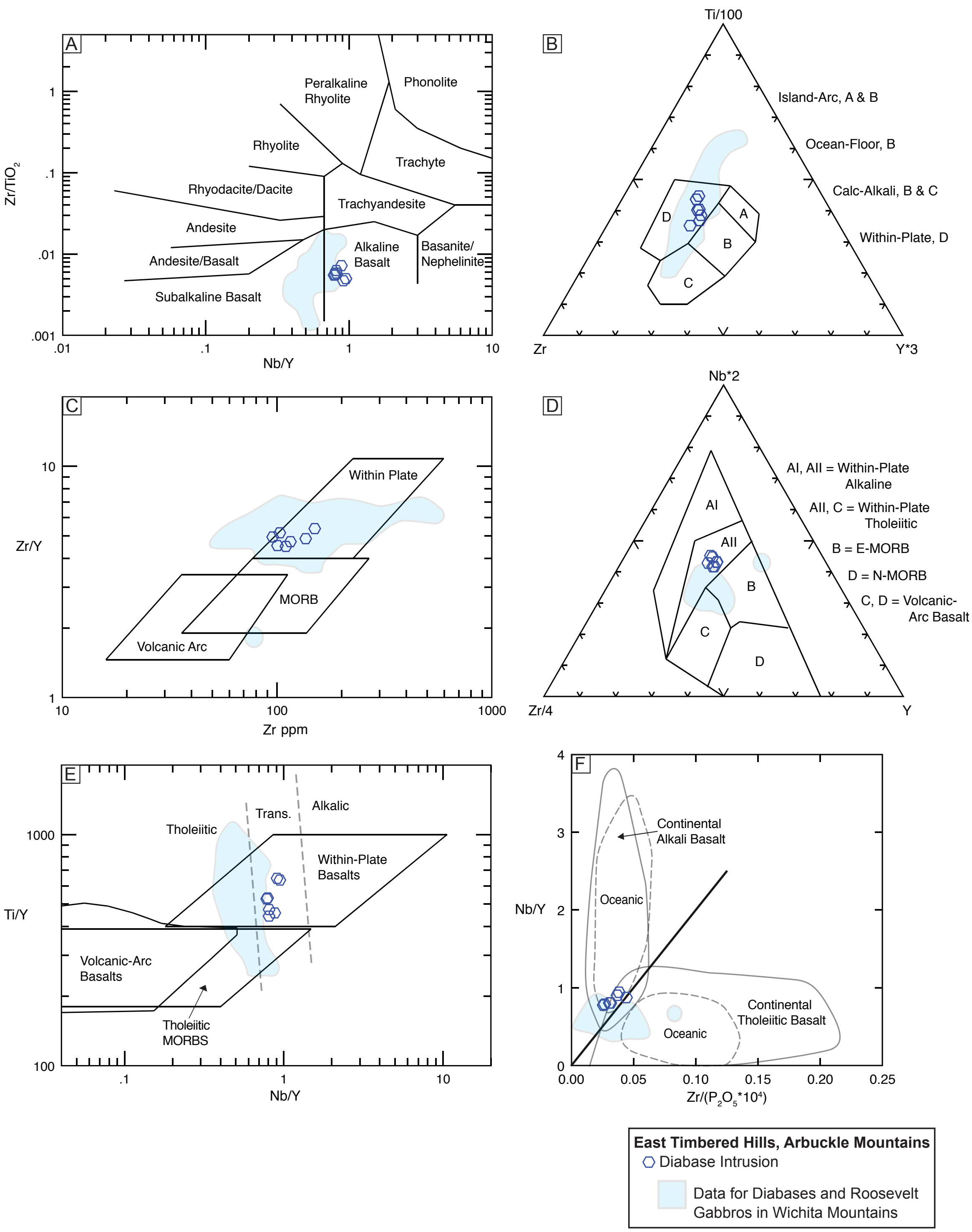

Figure 30. (A) Data for ETH diabase intrusions plotted on discrimination diagram of Winchester and Floyd (1977). (B) Zr-Ti-Y discrimination diagram of Pearce and Cann (1973). (C) Zr/Y versus Zr discrimination diagram of Pearce and Norry (1979). (D) Zr/4-Nb*2-Y discrimination diagram of Meschede (1986). (E) Ti/Y versus Nb/Y discrimination diagram of Pearce (1982). (F) Nb/Y versus Zr/(P_2O_5*10^4) discrimination diagram of Floyd and Winchester (1975). Data for diabase intrusions and Roosevelt gabbros in the Wichita Mountains are from sources given in caption for Figure 28.

Ham, W.E., and McKinley, M.E., 1954, Geologic Map and Sections of the Arbuckle Mountains, Oklahoma: Oklahoma Geological Survey Map A-2, 1 sheet, scale 1:72,000.

Hanson, R.E., Puckett, R.E., Jr., Keller, G.R., Brueseke, M.E., Bulen, C.L., Mertzman, S.A., Finegan, S.A., and McCleery, D.A., 2013, Intraplate magmatism related to opening of the southern Iapetus Ocean: Cambrian Wichita Igneous Province in the southern Oklahoma rift zone: Lithos, v. 174, p. 57-70.

Hughes, C.J., 1972, Spilites, keratophyres, and the igneous spectrum: Geological Magazine, v. 109, p. 513-527.

Johnson, K.S., 1990, Geologic Map and Sections of the Arbuckle Mountains, Oklahoma: Oklahoma Geological Survey Circular 91, Plate 1.

Le Bas, M.J., Le Maitre, R.W., Streckeisen, A., and Zanettin, B., 1986, A chemical classification of volcanic rocks based on the total alkali-silica diagram: Journal of Petrology, v. 27, p. 745-750.

Mahood, G., and Hildreth, W., 1983, Large partition coefficients for trace elements in high-silica rhyolites: Geochimica et Cosmochimica Acta, v. 47, p. 11-30.

Meschede, M., 1986, A method of discriminating between different types of mid-ocean ridge basalts and continental tholeiites with the Nb–Zr–Y diagram: Chemical Geology, v. 56, p. 207-218.

Pearce, J.A., 1982, Trace element characteristics of lavas from destructive plate boundaries, *in* Thorpe, R.S., ed., Andesites: Orogenic Andesites and Related Rocks: New York, Wiley, p. 525-548.

Pearce, J.A., and Cann, J.R., 1973, Tectonic setting of basic volcanic rocks determined using trace element analyses: Earth and Planetary Science Letters, v. 19, p. 290-300.

Pearce, J.A., and Norry, M.J., 1979, Petrogenetic implications of Ti, Zr, Y and Nb variations in volcanic rocks: Contributions to Mineralogy and Petrology, v. 69, p. 33-47.

Pearce, J.A., Harris, N.B.W., and Tindle, A.G., 1984, Trace element discrimination diagrams for the tectonic interpretation of granitic rocks: Journal of Petrology, v. 25, p. 956-983.

Perry, W.J., Jr., 1989, Tectonic Evolution of the Anadarko Basin Region, Oklahoma: U.S. Geological Survey Bulletin 1866A, 19 p.

Puckett, R.E., Jr., 2011, A thick sequence of rift-related basalts in the Arbuckle Mountains, Oklahoma, as revealed by deep drilling: Shale Shaker, v. 61, p. 207-217.

Reeds, C.A., 1910, A Report on the Geological and Mineral Resources of the Arbuckle Mountains, Oklahoma: Oklahoma Geological Survey Bulletin 3, 69 p.

Rohs, C.R., and Van Schmus, W.R., 2007, Isotopic connections between basement rocks exposed in the St. Francois Mountains and the Arbuckle Mountains, southern mid-continent, North America: International Journal of Earth Sciences, v. 96, p. 599-611.

Rollinson, H.R., 1993, Using Geochemical Data: Evaluation, Presentation, and Interpretation: Harlow, UK, Prentice Hall, 352 p.

Simons, F.S., 1962, Devitrification dikes and giant spherulites from Klondyke, Arizona: American Mineralogist, v. 47, p. 871-885.

Sun, S.S., and McDonough, W.F., 1989, Chemical and isotopic systematics of oceanic basalts; implications for mantle composition and process, *in* Saunders, A.D., and Norry M.J., eds., Magmatism in the Ocean Basins: Geological Society of London Special Publication No. 42, p. 313-345.

Taff, J.A., 1904, Preliminary Report on the Geology of the Arbuckle and Wichita Mountains in Indian Territory and Oklahoma: U.S. Geological Survey Professional Paper, v. 31, 97 p.

Thomas, W.A., Tucker, R.D., Astini, A.A., and Denison, R.E., 2012, Ages of pre-rift basement and synrift rocks along the conjugate rift and transform margins of the Argentine Precordillera and Laurentia: Geosphere, v. 8, no. 6, p. 1-18.

Uhl, B.F., 1932, Igneous rocks of the Arbuckle Mountains [M.S. thesis]: Norman, Oklahoma, University of Oklahoma, 54 p.

Whalen, J.B., Currie, K.L., and Chappell, B.W., 1987, A-type granites: Geochemical characteristics, discrimination and petrogenesis: Contributions to Mineralogy and Petrology, v. 95, p. 407-419.

Winchester, J.A., and Floyd, P.A., 1977, Geochemical discrimination of different magma series and their differentiation products using immobile elements: Chemical Geology, v. 20, p. 325-343.